Behavioral-transcriptomic landscape of engineered T cells targeting human cancer organoids

Authors:

Johanna F. Dekkers[1,2,3#], Maria Alieva[2,3#], Astrid Cleven[4], Farid Keramati[2], Peter Brazda[2], Heggert G. Rebel[2,3], Amber K.L. Wezenaar[2,3], Jens Puschhof[1,3], Maj-Britt Buchholz[2,3], Mario Barrera Román[2,3], Inez Johanna[4], Angelo D. Meringa[4], Domenico Fasci[4], Maarten H. Geurts[1,3], Hendrikus C.R. Ariese[2,3], Esmée J. van Vliet[2,3], Ravian L. van Ineveld[2,3], Effrosyni Karaiskaki[4], Oded Kopper[1,3], Yotam E. Bar-Ephraim[1,3], Kai Kretzschmar[1,3], Alexander M.M. Eggermont[2,5], Ellen J. Wehrens[2,3], Henk G. Stunnenberg[2], Hans Clevers[1,2,3±], Jürgen Kuball[4,6±], Zsolt Sebestyen[4±] and Anne C. Rios[2,3±]

# These authors contributed equally to this work

± These authors share senior authorship

Affiliations:

[1]Hubrecht Institute, Royal Netherlands Academy of Arts and Sciences (KNAW) and University Medical Centre (UMC) Utrecht, Utrecht, The Netherlands.

[2]Princess Máxima Center for Pediatric Oncology, Utrecht, The Netherlands.

[3]Cancer Genomics Netherlands, Oncode Institute, Utrecht, the Netherlands.

[4]Center for Translational Immunology, UMC Utrecht, Utrecht University, Utrecht, The Netherlands.

[5]UMC Utrecht, Utrecht, The Netherlands.

[6]Department of Hematology, UMC Utrecht, Utrecht University, Utrecht, The Netherlands

[*]Correspondence: a.c.rios@prinsesmaximacentrum.nl

Summary

Cellular immunotherapies are rapidly gaining clinical importance, yet predictive platforms for modeling their mode of action are lacking. Here, we developed a dynamic immuno-organoid 3D imaging-transcriptomics platform; BEHAV3D, to unravel the behavioral and underlying molecular mechanisms of solid tumor targeting. Applied to an emerging cancer metabolome-sensing immunotherapy: TEGs, we first demonstrate targeting of multiple breast cancer subtypes. Live-tracking of over 120,000 TEGs revealed a diverse behavioral landscape and identified a 'super engager' cluster with serial killing capability. Inference of single-cell behavior with transcriptomics identified the gene signature of 'super engager' killer TEGs, which contained 27 genes with no previously described T cell function. Furthermore, guided by a dynamic type 1 interferon (IFN-I) signaling module induced by high TEG-sensitive organoids, we show that IFN-I can prime resistant organoids for TEG-mediated killing. Thus, BEHAV3D characterizes behavioral-phenotypic heterogeneity of cellular immunotherapies and holds promise for improving solid tumor-targeting in a patient-specific manner.

Keywords:

BEHAV3D, multispectral time-lapse 3D imaging, behavioral classification, behavior-guided transcriptomics, patient-derived organoids (PDOs), breast cancer, T cell therapy, αβ T cells engineered to express a Vγ9/Vδ2 T cell receptor (TEGs), breast cancer, serial killing

47 **Introduction**

48 Single-cell analyses are providing unprecedented opportunities to analyze the complexity of
49 biological systems (van der Leun et al., 2020). However, they are restricted to providing a
50 snapshot of cellular processes at a given timepoint. Yet living cells are highly dynamic, and
51 their dynamic behavior shapes their function. Therefore, the development of technologies that
52 address individual cell dynamics within a population is essential for understanding cellular
53 behaviors and how these behaviors relate to function. Immune cells engineered to locate and
54 kill tumor cells represent such dynamic cell populations with an increasing clinical importance
55 (June and Sadelain, 2018). Successes of T cell therapies for hematological malignancies have
56 sparked efforts to translate such approaches to solid tumors, including breast cancer (BC), but
57 efficacy has so far been limited (Chen and Mellman, 2017). This poses a clear need for better
58 understanding the mechanism of action of cellular therapies in order to optimize treatment
59 design.

60

61 Because of challenges in identifying tumor-specific antigens for solid cancers (Schumacher et
62 al., 2019), pan-tumor therapies that recognize metabolic alterations in cancer cells are being
63 explored (Crowther et al., 2020). This includes an emerging therapy called TEGs, which are
64 peripheral blood αβ T cells engineered to express a Vγ9/Vδ2 T cell receptor (TCR), comprising
65 both $CD4^+$ and $CD8^+$ subsets (Gründer et al., 2012; Johanna et al., 2019; Marcu-Malina et al.,
66 2011; Sebestyen et al., 2019; Vyborova et al., 2020). These hybrid cells have the ability to
67 recognize cancer cells via the Vγ9/Vδ2 TCR that senses metabolic changes through the recently
68 identified ligand butyrophilin 2A1 (BTN2A1) bound to BTN3A1 (Rigau et al., 2020; Vyborova
69 et al., 2020). Yet, they maintain the high proliferation and memory capacity of conventional
70 αβ T cells (Marcu-Malina et al., 2011). TEGs are currently in clinical trials for various

leukemia (Sebestyen et al., 2019), but their potential to target solid tumors remains unknown and should be adressed in adequate preclinical models.

There is a growing interest to use organoid technology to model immunotherapy function (Bar-Ephraim et al., 2019; Cattaneo et al., 2020; Neal et al., 2018; Schnalzger et al., 2019; Dijkstra et al., 2018). Patient-derived organoids (PDOs) provide reliable *in vitro* human cancer models that recapitulate important characteristics of the original tumor specimen (Tuveson et al.), allowing for the study of patient-specifc therapy responses (Ganesh et al., 2019; Ooft et al., 2019; Tiriac et al., 2018; Vlachogiannis et al., 2018; Yao et al., 2020). In addition, imaging has proven to be a powerful approach to characterize the spatial cellular organization and tissue dynamics in these 3D structures (Dekkers et al., 2019; van Ineveld et al., *in press*; Lukonin et al., 2020; 2019; Serra et al., 2019). Here, we aim to combine organoid and 3D imaging technology for the analysis of functional single cell behavior integrated with transcriptomic profiling to decipher and manipulate the solid tumor-targeting strategy of engineered immune cells (**Video S1**).

Results

3D live-tracked TEG targeting efficacy

We devised a multispectral 3D image-based platform; BEHAV3D, to live-track efficacy and mode-of-action of cellular immunotherapy for ~60 human cancer organoid cultures simultaneously (**Figures 1A-1C; Video S1**). Multiple real-time fluorescent dyes and nanobody technology were implemented for single acquisition 4-fluorophore spectral 3D imaging of T cell populations, organoids, and dead cells, allowing us to track single TEGs, individual organoids and their death-dynamics over 24 h (**Figures 1B, 1C, and S1A-S1C**). We detected

96 a high variation of TEG-mediated killing efficacy in cultures derived from 14 BC patients
97 (**Figure 1D; Table S1**), and different targeting kinetics over time (**Figures 1E, 1F, and S1D-**
98 **S1F**), with percentages of dying PDOs ranging from near 0% (e.g. 34T) to 100% (e.g. 13T)
99 (**Figure 1F**). Pearson correlation analysis between imaging data and a commonly used cell
100 viability assay **(Figures S1G and S1H)**, or interferon gamma (IFN-γ) secretion measured by
101 ELISA **(Figures S1I and S1J)**, confirmed robustness of our imaging quantification method.
102 Among the 6 highest TEG-sensitive PDO cultures (above 50% dying organoids; **Figure 1F**),
103 we noted cultures derived from primary BC of distinct subtypes (triple negative breast cancer
104 (TNBC), human epidermal growth factor receptor 2 $(HER2)^+$, estrogen receptor $(ER)^+$, and
105 ER^+ progesterone receptor $(PR)^+HER2^+$) and from a metastasis derived from a $HER2^+$ primary
106 tumor (**Figures 1D and 1F**), supporting the potential of TEGs in targeting a broad spectrum of
107 BCs. Importantly, TEGs control the growth of PDO-derived breast tumors (TNBC primary
108 tumor and $HER2^+$ metastasis) in mouse xenograft models (**Figure 1G**), showing efficacy of
109 TEG for BC *in vivo*.
110
111 **PDO inflammatory features associate with TEG sensitivity**
112 Bulk RNA sequencing of PDOs revealed differentially expressed genes (DEGs) between the 6
113 lowest versus the 6 highest TEG-sensitive PDO cultures (**Table S2**), related to upregulated
114 cadherin signaling and steroid biosynthesis pathways in TEG-insensitive cultures, whereas
115 cytokine signaling, as well as extracellular matrix (ECM) organization, correlated with high
116 sensitivity to TEG therapy (**Figures 1H, and S1K-S1M**). The highest association was found
117 between TEG killing and type 1 interferon (IFN-I) signaling genes, including MX1, IFIT1,
118 OASL, and XAF1, which were highly expressed especially in the 2 highest TEG-sensitive PDO
119 cultures; 14T and 13T (**Figures 1H, and S1M)**. Thus, PDOs maintain tumor-specific

120 inflammatory features in culture, highlighting their utility for modeling cellular
121 immunotherapy responses in a patient-specific manner.
122
123 **TEGs display a high diversity in behavior and killing potential**
124 BEHAV3D implements single immune cell tracking in a 3D space over time and behavioral
125 classification (**Figures 1B, and 2A; Video S1**), revealing that -when exposed to PDOs- TEGs
126 could be separated into nine subpopulations with unique behavioral patterns (**Figures 2B-2D,**
127 **and S2A, S2B**). Patterns varied from inactive behaviors (*dying*, *static* and *lazy*) to active
128 motility (*slow scanner*, *medium scanner* and *super scanner*) and organoid engagement (*tickler*,
129 *engager* and *super engager*), thus demonstrating a high level of behavioral heterogeneity.
130 Having captured their behavioral single-cell landscape in this classifier (**Figures S3C-S3E)**,
131 we next predicted TEG behavior when co-cultured with PDOs that showed varying TEG
132 sensitivity (34T, 100T, 27T, 10T or 13T; **Figure 1F**), as well as an organoid culture derived
133 from normal breast tissue, which only showed minimal death when cultured with TEGs
134 (**Figure 2E**). A total of 123,296 TEGs were live-tracked to investigate how the organoid
135 (inflammatory) profile shapes T cell behavior. For each PDO culture, TEGs displayed unique
136 distributions of behavioral signatures (**Figure 2E**) and higher organoid killing associated with
137 an increase in tumor engagement (*tickler*, *engager* and *super engager*), while *static, lazy* and
138 *medium scanner* behavior decreased (**Figure 2F**). Correlation between single organoid dying
139 dynamics and TEG engagement over time revealed that organoids contacted by *super*
140 *engagers*, as compared to other organoid-engaging clusters, had the highest chance of being
141 killed (**Figures 2G, and S2F).** This indicates that effective killing by TEGs relies on prolonged
142 organoid contact, a main feature of *super engagers* (48 ± 8 min / hr; mean ± s.d.).
143
144 **Serial killing capability of *super engager* CD8$^+$ TEGs**

145 We next linked behaviors to population phenotypes by first differentially labeling $CD4^+$ and
146 and $CD8^+$ T cells **(Figures 3A, and S3A**). This revealed that prolonged organoid contact and
147 *super engager* behavior was a preferred feature of $CD8^+$ TEGs, whereas $CD4^+$ TEGs showed
148 a higher proportion of *lazy* cells, *slow scanners*, *medium scanners*, *super scanners*, and *ticklers*
149 (**Figures 3A-3C)** characteristic of high movement and short organoid contact (**Figure 2C**).
150 Furthermore, long-term behavior classification and back-projection of cells classified in the
151 live-tracked imaging dataset (**Figures S3B and S3C**), showed that single $CD8^+$ TEGs, once
152 engaged with an organoid, most often killed multiple cells consecutively (serial killing)
153 (**Figures 3D-3G**), a preferred feature of engineered T cells(Cazaux et al., 2019; Halle et al.,
154 2016; Weigelin et al.). In contrast, $CD4^+$ TEGs often moved away after organoid engagement
155 without killing, but occasionally targeted individual cells in different organoids (**Figures 3D-**
156 **3F, and S3D**) thereby displaying slower killing rates (**Figure 3H**). Serial killing by *super*
157 *engager* $CD8^+$ TEGs was characterized by attachment to PDOs using a defined anchor point
158 from where surrounding cells were killed via long protrusions, intercalating between epithelial
159 cells and extending their initial size up to 5 times (**Figures 3E, and S3E and S3F**).
160 Remarkably, single $CD8^+$ TEGs were able to kill entire organoids (up to 18 cells in 11 hrs;
161 **Figures 3E and 3G; Video S1**). This extent of serial killing and morphological plasticity of
162 *super engager* $CD8^+$ TEGs was uniquely revealed by the high spatiotemporal resolution
163 character of BEHAV3D.
164
165 **NCAM1 associates with *super engager* behavior**
166 Through single cell RNA sequencing (scRNAseq), we observed differential expression of
167 NCAM1 in $CD8^+$ TEGs (**Figures 3I**, **S3G and S3H; Table S3**). Although linked to
168 cytotoxicity in both αβ and γδ T cells(Van Acker et al., 2017), this surface marker has not been
169 examined in the context of cellular immunotherapy. We confirmed potent effector function

170 related to NCAM1 expression, by showing that NCAM1^{+}CD8^{+} TEGs had a higher capacity to
171 kill 13T organoids compared to NCAM1^{-}CD8^{+} TEGs (**Figure 3J**). To identify behavioral
172 mechanisms underlying this high killing potential, we pre-labeled CD8^{+} TEGs with NCAM1
173 nanobodies (**Figure 3K)**, to directly compare NCAM1-positive and -negative populations
174 within the same environment. NCAM1^{+}CD8^{+} TEGs showed reduced *dying* and *static* behavior
175 (**Figures 3L and 3M, and S3I**), supporting a higher *in vitro* persistence. Strikingly,
176 NCAM1^{+}CD8^{+} TEGs additionally showed a significant increase in *super engager* behavior
177 compared to NCAM1^{-}CD8^{+} TEGs (**Figure 3L and 3M**). Thus, surface marker expression can
178 be linked to engineered T cell behavior, offering the opportunity to enrich for potent effector
179 behaviors.
180
181 **Behavioral-transcriptomic profiling of TEGs**
182 To generate insight into the transcriptional programs that underlie tumor-targeting dynamics
183 revealed by BEHAV3D, we next performed single cell transcriptomic profiling of TEG
184 populations enriched for different behavioral signatures, including a TEG population
185 containing > 90% *super engagers* (**Figures 4A and 4B, and S4A; Video S1**). For each main
186 TEG subset, effector CD8^{+} (CD8^{+eff}), effector CD4^{+} (CD4^{+eff}) and memory CD4^{+} (CD4^{+mem}),
187 profound transcriptional changes were observed upon 6 h co-culture with highly targeted 13T
188 organoids, as compared to baseline (*no target control*) (**Figures 4C-4E**), showing that dynamic
189 interplay with PDOs shapes the TEG transcriptomic profile. Behavioral probability mapping
190 inferred from pseudotemporal ordering (**Figure S4B**) of the sequenced TEG populations
191 (**Figure 4F**), revealed dynamic transcriptional programs that were highly conserved between
192 CD8^{+eff}, CD4^{+eff}, and CD4^{+mem} TEGs (**Figure 4G**; Gene cluster (CL)1-3; 85% of genes; **Table**
193 **S4**). These programs included genes to be down- (CL1) or up-regulated (CL3) by
194 environmental stimuli or engagement to PDOs, as well as genes transiently expressed (CL2)

195 along the pseudotime trajectory (**Figure 4G;** GO terms per CL in **Figure S4C**). This
196 differential dynamic expression matched with known gene function, confirming robust
197 ordering of TEGs, as shown by genes related to the CD3 signaling complex (LCK, SOS1,
198 CD3E, CD3G; CL1; GO term 'T cell activation'), known to be down-regulated upon T cell
199 activation(Liu et al., 2000) in CL1 (**Figure 4H)**. NF-kB signaling, critical for tumor
200 control(Barnes et al., 2015), and effector molecules including FASLG, IFNG, GZMB, TNF
201 were found in CL3, with NF-kB signalling induced by environmental stimuli reaching
202 maximum expression upon prolonged PDO-engagement, while the effector molecules
203 appeared upon engagement (**Figure 4I**). In addition, CL3 contained genes related to rRNA
204 processing that only increased upon prolonged engagement with organoids (**Figure 4H**),
205 consistent with accelerated protein production in T cells following TCR engagement(Asmal et
206 al., 2003; Tan et al., 2017). Finally, CL2 contained early activation markers CD69 and EGR1
207 with peak expression upon short organoid engagement, in line with IL-2 (CL3), known to be
208 induced by EGR1(Collins et al., 2006), upregulated towards the end of the trajectory (**Figure**
209 **4I**). Thus, through our behavior-guided transcriptomics approach we robustly identified
210 dynamic gene orchestration of TEG during tumor targeting.
211
212 **Gene signature related to (serial) killing *super engager* TEGs**
213 Of gene sets regulated in a TEG subset-specific manner (CL4-8; 15% of genes), CL7 contained
214 genes mainly induced upon prolonged organoid engagement, including cytotoxic genes (e.g.
215 PRF1, CRTAM, XCL1) (**Figures 4H and 4I;** GO: 'Regulation of cell killing'). This cluster of
216 genes was specifically induced in *super engager* $CD8^{+eff}$, and to a lesser extent in $CD4^{+eff}$
217 TEGs, and almost absent in $CD4^{+mem}$ TEGs (**Figure 4J**), associating this gene cluster with
218 potent (serial) killing T cells (**Figures 3D-3G**). Analysis of TEGs derived from a different
219 healthy donor and co-cultured with another PDO culture (10T), confirmed that 61 out of the

220 83 genes of CL7 represent a conserved 'killer' gene signature (**Table S5**). Of these, we
221 identified 20 genes related to T cell activation and cytotoxicity and 14 genes related to other T
222 cell functions (**Figures 4K, and S4D**). However, importantly, we found 27 genes with no
223 previously described T cell function (**Figures 4K, and S4D**). Overall, half of all conserved
224 signature genes (31/61) and 17 out of the 27 novel genes were related to morphological
225 plasticity processes, such as motility, cytoskeleton remodeling and adhesion (**Figure S4D**).
226 Given that morphological plasticity is a key determinant of cell migration, many of the novel
227 genes were found to have a role in promoting tumor cell migration and invasion, including
228 ECM production and mesenchymal state induction (HEG1, BZW2, DCAF13, SQLE, PKIA).
229 For some of these genes, such as CCT3 or AFAP1L2, the mechanism promoting migration is
230 yet undescribed. In line with the prolonged organoid engagement behavioral feature of *super*
231 *engager* TEGs (**Figure 2C**), we also found various genes related to cell adhesion, such as
232 NCEH1, BYSL or EMP1. Finally, some genes had an additional function related to neurite
233 outgrowth and dendritic pruning (SERPINE2, CHD4, NRTK1), potentially matching the long
234 protrusion that were observed to occur in these serial killing TEGs **(Figures 3E, and Figure**
235 **S3E and S3F; Video S1).** Thus, behavioral transcriptomics identified a specific gene signature
236 induced in (serial) killing *super engager* TEGs.
237
238 **PDOs shape the dynamic gene signature of TEG during tumor targeting**
239 To further explore our behavioral-guided transcriptomics approach, we next compared
240 behavior-enriched TEG populations co-cultured between either highly sensitive 13T or
241 intermediately targeted 10T PDOs. Distinct UMAP embedding of different TEG populations
242 (**Figure 5A**) indicated that the patient-specific organoid exposure influences the dynamic TEG
243 transcriptional profile. 41% or 61% of upregulated genes by environmental stimuli or upon
244 prolonged PDO engagement in *super engagers*, respectively, were common between 10T- and

245 13T-co-cultured TEGs (**Figures 5B**, **and S5A and S5B**; **Table S6)**. Common *super engager*-
246 related gene signatures included rRNA processing, NF-kB signaling and cytokine signaling
247 (**Figure S5B**), and matched CL3 gene signatures (**Figure S4C**). However, 10T-co-cultured
248 TEGs were characterized by induction of high cytokine expression upon prolonged PDO
249 engagement, including TNF, IFNG and IL2, whereas IFN-I signaling genes were uniquely
250 induced in TEGs co-cultured with highly sensitive 13T (**Figures 5C, and S5C**).
251

252 **IFN-β primes PDOs for TEG mediated killing**

253 IFN-I signaling plays fundamental roles in anti-tumor immunity, yet with diverse and
254 sometimes opposing functions reported for both tumor and immune cells, thereby making it
255 difficult to fully comprehend and therapeutically exploit these effects(Boukhaled et al., 2021).
256 IFN-I signaling was detected in 13T organoids (**Figure S1M**), which most prominently
257 displayed increased RNA levels of the upstream mediator IFN-β, but not IFN-α, among our
258 collection of PDOs (**Figure 5D)**. Secretion of IFN-β was confirmed by Luminex (**Figure S5D**),
259 implying that IFN-β was the main mediator of IFN-I signaling observed in 13T. Interestingly,
260 peak induction of IFN-I signaling in 13T-co-cultured TEGs was detected in non-organoid-
261 engaging TEGs (from *static* to *super scanner* behavior), in line with a secreted source of IFN-
262 β, while the pathway was shut down in *super engager* TEGs, suggesting a limited role of IFN-
263 I signaling in direct killing behavior (**Figures 4F-4H**). Adding recombinant IFN-β to co-
264 cultures of TEGs with various PDOs that showed low to medium sensitivity to TEG therapy
265 (100T, 34T, 27T and 10T) indeed did not affect TEG targeting efficacy (**Figure 5E**). However,
266 34T, 27T and 10T organoids pre-treated with IFN-β showed increased TEG-mediated killing,
267 while IFN-β treatment did not impact organoid viability by itself (**Figures 5F and 5G**). These
268 data support that IFN-β has limited impact on the killing capacity of *super engager* TEGs,
269 confirming that dynamic IFN-I signaling is mainly associating with *static* to *scanner* behavior.

270 Importantly however, IFN-I signaling increases the sensitivity of organoids to TEG therapy.
271 Thus, behavior-guided TEG transcriptomics in relation to the type of organoid exposure reveals
272 IFN-β to prime PDOs for targeting by TEGs. This illustrates the potential of the BEHAV3D to
273 better understand and guide combinatory treatment approaches in a patient-specific manner.
274
275

Discussion

Here, we provide an organoid-based 3D imaging-transcriptomic platform; BEHAV3D, for understanding the mode-of-action of cellular anti-cancer immunotherapies in a patient-specific manner. Using this pipeline, we report on the broad targeting potential of TEGs for breast cancer, poorly permissive to current immunotherapies (Esteva et al., 2019). In addition, by behavior-guided transcriptomics we have generated, to our knowledge, the first molecular map underlying the behavioral landscape of immune cells targeted to solid tumors. By exploiting these results, we were able to design an optimal sequence of IFN-I and TEG combination therapy to boost TEG organoid targeting.

Different from recent studies that have mapped the activation trajectories of murine immune cells during viral infection (Abbas et al., 2020), or human immune cells in normal physiology or cancer (Szabo et al., 2019), we here reconstructed activation trajectories for engineered T cells and uniquely exploited dynamic imaging data revealing their single-cell behavior. This allowed us to dissect gene programs induced by environmental stimuli, versus induction by short or prolonged tumor engagement, and thereby identify the gene signature of TEGs that (serially) killed tumor cells. This signature includes genes not previously linked to T cell function, thereby providing novel opportunities to potentially engineer next generation T cells with potent serial killing capability. Furthermore, multiple genes in this signature-are associated with morphological plasticity. Such plasticity may underlie the remarkable cellular extensions of serial-killing TEGs, as observed in our 3D imaging data. Using these protrusions, TEGs intercalate~~d~~ between tumor cells while sequentially killing multiple tumor cells in the PDO, suggesting that morphological plasticity may be an important attribute in the targeting of solid tumors.

299 Type 1 IFNs have been described to be beneficial for the control of tumor growth,
300 including in breast cancer, either by exerting direct antitumor effects (Dunn et al., 2005), or by
301 improving the response to therapies, such as chemotherapy and checkpoint inhibition (Borden,
302 2019; Sistigu et al., 2014). Yet, opposite roles in inducing treatment resistance have been
303 described as well (Benci et al., 2016; Boukhaled et al., 2021; Jacquelot et al., 2019). By using
304 defined immune-organoid co-cultures, we have shown that an IFN-I signature intrinsic to
305 tumor cells associates with TEG sensitivity, and that IFN-β primes tumor cells for more
306 efficient targeting, rather than directly affecting TEG killing behavior. Thus, our data support
307 the clinical use of IFN-I in combination with TEGs and possibly other cellular
308 immunotherapies.

309 Adding to patient-specific drug responses observed in PDOs biobanks (Ganesh et al.,
310 2019; Jacob et al., 2020; Ooft et al., 2019; Tiriac et al., 2018; Vlachogiannis et al., 2018; Yao
311 et al., 2020), we show that not only killing efficacy, but also the underlying behavioral and
312 molecular mechanisms of cellular immunotherapy differ between different PDO cultures. We
313 even detected differences in killing dynamics between individual organoids belonging to the
314 same PDO culture. This demonstrates that our platform captures the inter- and intra-patient
315 heterogeneity, a major obstacle for treating solid tumors (Yamamoto et al., 2019). It is
316 intriguing that gene signatures induced in TEGs upon organoid engagement were partly
317 dictated by the type of PDO. In addition, the extent of IFN-β pre-treatment outcome on tumor
318 targeting differed between PDOs, with the highly resistant culture 100T remaining
319 unresponsive, whereas 34T displayed the highest (4-fold) increase in targeting. Together, these
320 findings warrant caution regarding generalizing the outcome of immuno-oncology studies that
321 use a single tumor model, and further supports the value of human organoid technology for
322 development of personalized therapies.

Altogether, BEHAV3D combines organoid, imaging and sequencing technologies to offer a comprehensive platform that integrates multiple single-cell readouts, including tumor death dynamics, single-cell behavior and underlying transcriptomic profiling (**Video S1**). BEHAV3D may thus contribute to the efforts aimed at enhancing the efficacy of solid tumor-targeting by cellular therapies.

330 **Methods**

331

332 **Human material**

333 All human PDO samples were retrieved from a biobank through the Hubrecht Organoid
334 Technology (HUB, www.hub4organoids.nl). Authorizations were obtained by the medical
335 ethical committee of UMC Utrecht (METC UMCU) at request of the HUB in order to ensure
336 compliance with the Dutch medical research involving human subjects' act. The normal
337 organoids were generated from milk obtained via the Moedermelkbank Amsterdam
338 (Amsterdam UMC). Informed consent was obtained from all donors.

339

340 **Animal material**

341 NOD.Cg-PrkdcscidIl2rgtm1Wjl/SzJ (NSG) mice purchased from Charles River Laboratories
342 (France). Experiments were conducted in accordance with Institutional Guidelines under
343 acquired permission from the local Ethical Committee and as per current Dutch laws on Animal
344 Experimentation. Mice were housed in sterile conditions using an individually ventilated cage
345 (IVC) system and fed with sterile food and water. Irradiated mice were given sterile water with
346 antibiotic ciproxin for the duration of the experiment. Mice were randomized with equal
347 distribution by age and initial weight measured on day 0 and divided into 10–15 mice per
348 group.

349

350 **Organoid culture**

351 Organoids were seeded in basement membrane extract (BME; Cultrex) in uncoated 12-well
352 plates (Greiner Bio-one) and cultured as described previously(Dekkers et al., 2021; Sachs et
353 al., 2017). Briefly, Advanced DMEM/F12 was supplemented with penicillin/streptomycin
354 (pen/strep), 10 mM HEPES, Glutamax (adDMEM/F12+++), 1 x B27 (all from Thermo Fisher),

355 1.25 mM N-acetyl-L-cysteine (Sigma-Aldrich), 10 mM Nicotinamide (Sigma-Aldrich), 5 µM
356 Y-27632 (Abmole), 5 nM Heregulin β-1 (Peprotech), 500 nM A83-01 (Tocris), 5 ng/ml EGF
357 (Peprotech), 20 ng/ml FGF-10 (Peprotech), 10% Noggin-conditioned medium (NCM)
358 (Cattaneo et al., 2020), 10% Rspo1-conditioned medium (RCM) (Broutier et al., 2016), and
359 0.1 mg/ml primocin (Thermo Fisher), and in addition with 1 µM SB202190 (Sigma-Aldrich)
360 and 5 ng/ml FGF-7 (Peprotech) for PDO propagation ('Type 1' culture medium(Dekkers et al.,
361 2021)), or with 20% Wnt3a-conditioned medium (WCM) (Broutier et al., 2016), 0.5 µg/ml
362 hydrocortisone (Sigma-Aldrich), 100 µM β-estradiol (Sigma-Aldrich) and 10 mM forskolin
363 (Sigma-Aldrich) for normal organoid propagation ('Type 2' culture medium (Dekkers et al.,
364 2021)). Culture medium was refreshed every 2–3 days and organoids were passaged 1:2–1:6
365 every 7–21 days using TrypLE Express (Thermo Fisher). For co-culturing, organoids of a 5–
366 12-day old culture (depending on PDO growth speed) were recovered from the BME by
367 resuspension in TrypLE Express and collected adDMEM/F12+++. The organoid suspension
368 was filtered through a 70 µm strainer (Greiner) to remove large organoids and pelleted before
369 co-culturing. Organoids of passage 5 to 30 after cell isolation were used.
370
371 **Cell lines**
372 Daudi (Gründer et al., 2012), HL60(Marcu-Malina et al., 2011) and Phoenix-Ampho cell lines
373 were obtained from ATCC (authenticated by short tandem repeat
374 profiling/karyotyping/isoenzyme analysis). Daudi and HL60 cells were cultured in RPMI
375 media supplemented with 10% fetal calf serum (FCS) and 1% pen/strep (all from Thermo
376 Fisher). Phoenix-Ampho cells were cultured in DMEM medium (Thermo Fisher)
377 supplemented with 10% FCS and 1% pen/strep. All cells were passaged for a maximum of 2
378 months, after which new seed stocks were thawed for experimental use. Furthermore, all cell
379 lines were routinely verified by growth rate, morphology, and/or flow cytometry and tested

380 negative for mycoplasma using MycoAlert Mycoplasma Kit. Peripheral blood mononuclear
381 cells (PBMCs) were obtained from Sanquin Blood bank (Amsterdam, The Netherlands) and
382 isolated using Ficoll gradient centrifugation methods from buffy coats.

383 **Retroviral transduction of T cells**

384 TEG001 (T cells engineered to express a highly tumor-reactive Vγ9Vδ2 TCR) (Gründer et al.,
385 2012; Straetemans et al., 2015; 2018), LM1s (mock T cells engineered to express a mutant
386 Vγ9/Vδ2 TCR with abrogated function) (Marcu-Malina et al., 2011), and TEG011 (mock T
387 cells engineered to express HLA-A*24:02-restricted Vγ5/Vδ1 TCR; used as control for *in vivo*
388 studies) (Kierkels et al., 2019; Scheper et al., 2013), were produced as previously described
389 (Marcu-Malina et al., 2011). Briefly, packaging cells (Phoenix-Ampho) were transfected with
390 helper constructs gag-pol (pHIT60), env (pCOLT-GALV) and pMP71 retroviral vectors
391 containing both Vγ9/Vδ2 TCR chains separated by a ribosomal skipping T2A sequence, using
392 FugeneHD reagent (Promega). Human PBMCs from healthy donors were pre-activated with
393 anti CD3 (30 ng/mL; Orthoclone OKT3; Janssen-Cilag) and IL-2 (50 IU/mL; Proleukin,
394 Novartis) and subsequently transduced twice with viral supernatant within 48 hrs in the
395 presence of 50 IU/mL IL-2 and 6 mg/mL polybrene (Sigma-Aldrich). TCR-transduced T cells
396 were expanded by stimulation with anti-CD3/CD28 Dynabeads (500,000 beads/10^6 cells; Life
397 Technologies) and IL-2 (50 IU/mL). Thereafter, TCR-transduced T cells were depleted of the
398 non-engineered T cells.
399

400 **Depletion of non-engineered T cells**

401 Depletion of non-engineered T cells was performed as previously described (Marcu-Malina et
402 al., 2011). In short, αβ T cells were transduced with pMP71: γ-T2A-δ and incubated with a
403 biotin-labelled anti-αβ TCR antibody (clone BW242/412; Miltenyi Biotec) followed by

404 incubation with an anti-biotin antibody coupled to magnetic beads (anti-biotin MicroBeads;
405 Miltenyi Biotec). Next, the cell suspension was applied onto an LD column and αβ TCR-
406 positive (αβ TCR^+) T cells were depleted by Magnetic-Activated Cell Sorting (MACS)
407 according to the manufacture's protocol (Miltenyi Biotec).
408
409 **Separation of $CD4^+$ and $CD8^+$ subsets of TEGs**
410 In order to separate $CD4^+$ and $CD8^+$ TEGs and LM1s, we performed positive selection using
411 either CD4 or CD8 Microbeads (Miltenyi Biotech) following manufacturer's instructions.
412 After incubation with magnetic microbeads cells were applied to LS columns and $CD4^+$ or
413 $CD8^+$ TEGs or LM1s were selected by MACS. After MACS selection procedure, both
414 Vγ9/Vδ2 TCR^+ $CD4^+$ or Vγ9/Vδ2 TCR^+ $CD8^+$ subsets of TEGs were separately expanded by
415 using a rapid expansion protocol (REP) (Marcu-Malina et al., 2011) where TEGs were cultured
416 in 'TEG culture medium' (RPMI-Glutamax supplemented with 2,5 – 10 % human serum
417 (Sanquin), 1% pen/strep and 0.5M beta-2- mercaptoethanol) on a feeder cell mixture
418 composing of irradiated allogenic PBMCs, Daudi and LCL-TM in the presence of IL2 (50
419 U/ml; Novartis Pharma), IL15 (5 ng/ml; R&D Systems) and PHA-L (1 μg/ml; Sigma-Aldrich).
420 TEGs were stimulated biweekly by using the REP protocol. In order to monitor the purity of
421 $CD4^+$ and $CD8^+$ TEGs, cells were analyzed by flow cytometry weekly prior to functional
422 assays by using anti-pan γδ TCR-PE (Beckman Coulter), anti- αβTCR-FITC (eBioscience),
423 anti-CD8-PerCP-Cy5.5 (Biolegend) and anti-CD4-APC (Biolegend) antibodies. TEGs with a
424 purity lower than 90% were re-selected as described above. TEGs were used for co-culture
425 assays 4 – 5 days after the last IL2/IL15/PHA-L stimulation.
426
427 **Sorting of $NCAM1^{-/+}$ TEGs**

428 $CD8^+$ TEGs were harvested at day 8-10 of their REP cycle, stained in flow cytometry (FC)
429 buffer (2% fetal bovine serum, 1x PBS) with Hilyte-488-conjugated NCAM1 nanobodies
430 (1:400; QVQ) and LIVE/DEAD Fixable Near-IR Dead Cell Stain (1:1000; ThermoFisher) for
431 30 minutes at 4˚C and consecutively sorted using a SONY SH800S or a FACS Aria Cell Sorter
432 (BD Biosciences) into $NCAM1^-$ and $NCAM^+$ populations. Cells were rested for 16 h in 'TEG
433 culture medium' and then used for co-culture.
434
435 **Live cell imaging of TEG and organoid co-cultures**
436 LM1s or TEGs (20,000) were co-cultured with normal organoids, PDOs or control cell lines
437 (Daudi or HL-60) in an effector to tumor cell (E:T) ratio of 1:3 or 1:25 (for **Figures 3D-3F**).
438 $CD4^+$ and $CD8^+$ TEGs were mixed in a 1:1 ratio just before plating. Cells were incubated in
439 96-well glass-bottom SensoPlates (Greiner) in 200 µl 'co-culture medium': 50% 'Type 1'
440 organoid culture medium, 50% 'TEG assay medium' (RPMI-Glutamax supplemented with
441 10% FCS and 1% pen/strep), 2.5% BME and pamidronate for the accumulation of the
442 phosphoantigen IPP to stimulate tumor cell recognition(Marcu-Malina et al., 2011) (1:2000).
443 'Co-culture medium' was supplemented with both NucRed™ Dead 647 (2 drops per ml;
444 Thermo Fisher) and TO-PRO-3 (1:3000; Thermo Fisher) for fluorescent labelling of living and
445 dead cells ('Imaging medium'). Combination of NucRed™ Dead 647 and TO-PRO-3 light up
446 dead cell when excited with the 633 nm laser, and living cells when excited with the 561 nm
447 laser (**Figures S1A and S1B**). Both were combined to achieve the most optimal fluorescent
448 intensity ratio between dead and living cells for live cell imaging. Prior to co-culturing, TEGs
449 were incubated with eBioscience™ Cell Proliferation Dye eFluor™ 450 (referred to as eFluor-
450 450; 1:4000; Thermo Fisher) in PBS for 10 min at 37 °C to fluorescently label all TEGs. When
451 $CD4^+$ and $CD8^+$TEGs were simultaneously imaged, eFluor-450, as well as Calcein AM
452 (1:4000; Thermo Fisher) were used to label the different TEG subsets in PBS for 10 min at 37

453 °C. For NCAM1 pre-labeling experiments, a combination of eFluor-450 (1:4000; Thermo
454 Fisher) and Hilyte-488-conjugated NCAM1 nanobodies (1:400; QVQ) was used to label $CD8^+$
455 TEGs in PBS for 20 min at 37 °C prior to co-culturing. To prevent evaporation while imaging,
456 200 µl PBS was added to the wells surrounding the co-culture wells. The plate was placed in a
457 LSM880 (Zeiss) microscope containing an incubation chamber (37 °C; 5% CO_2) and incubated
458 for 30 min to ensure settling of TEGs and organoids at the bottom of the well. The plate was
459 imaged for up to 24 hrs with a Plan-Apochromat 20 x/0.8 NA dry objective with the following
460 settings: online fingerprinting mode, bidirectional scanning, optimal Z-stack step size, Z-stack
461 of 60 µm in total and time series with a 30 min (up to 60 conditions simultaneously; resolution
462 512 x 512) or 2 min interval (up to 4 or 10 conditions simultaneously; resolution 512 x 512 and
463 200 x 200 respectively). To minimize photobleaching of NCAM1-pre-labeled TEGs, the 488
464 nm laser was only activated 1 Z-stack each hr within the first hrs of imaging. Directly after
465 imaging, the production of IFN-γ in the supernatant was quantitated using an ELISA-ready-
466 go! Kit (eBioscience) and cell pellets were used to measure organoid viability using a CellTiter-
467 Glo® Luminescent Cell Viability Assay (Promega).
468
469 **IFN-β stimulations**
470 PDOs were harvested as described above and incubated in 96-well round bottom culture plates
471 (Thermo Fisher) in 100 µl 'Type 1' organoid culture medium, supplemented with 2.5% BME,
472 with or without the presence of 100 pg/ml recombinant human IFN-β (Peprotech). After 24 h
473 incubation (37 °C; 5% CO_2), TEGs or LM1s were added to either IFN-β-preincubated or
474 unstimulated organoids (E:T ratio of 1:3) in 100 µl 'TEG assay medium', supplemented with
475 2.5% BME and pamidronate (1:1000), with or without the presence of 100 pg/ml recombinant
476 human IFN-β (Peprotech). Medium without T cells was added for 'organoid only' controls.

477 After 16 h incubation (37 °C; 5% CO_2), plates were used to measure organoid viability using
478 a CellTiter-Glo® Luminescent Cell Viability Assay (Promega).
479
480 ***In vivo* targeting by TEGs**
481 Adult female NSG mice (15-16 weeks old) received sub-lethal total body irradiation (1,75 Gy)
482 and subcutaneous implantation of an β-estradiol pellet (Innovative Research of America) on
483 Day -1. On day 0, PDOs ($1x10^6$ 13T organoid cells in 100 µl BME per mouse) were prepared
484 as described previously (Dekkers et al., 2021) for subcutaneous injection on the right flank on
485 Day 0, and received 2 injections of 10^7 TEGs or TEG011 mock cells on day 1 and 6 in
486 pamidronate (10 mg/kg body weight) as previously reported(Johanna et al., 2019). On day 1,
487 together with the first T cell injection, all mice also received $0.6x10^6$ IU of IL-2 (Proleukin;
488 Novartis) in IFA subcutaneously. Tumor volume was measured once a week using digital
489 caliper and was calculated by the following formula: 0.4 x (length x width x width). Mice were
490 monitored at least twice a week for weight loss and clinical appearance scoring (scoring
491 parameter included hunched appearance, activity, fur texture, piloerection,
492 respiratory/breathing problem). Humane endpoint (HEP) was reached when mice experienced
493 a 20% weight loss from the initial weight, tumor volume reached 2 cm^3, or when clinical
494 appearance score of 2 was reached for individual parameter or an overall score of 4.
495
496 **Image processing**
497 For 3D visualization, cell segmentation and extraction of statistics, time-lapse movies were
498 processed with Imaris (Oxford Instruments), versions 9.2 to 9.5. The *Channel Arithmetics*
499 Xtension was used for creating new channels to specifically identify organoids (live and dead)
500 and eFluor-450-labeled or calcein AM-labeled TEGs (live and dead) and exclude cell debris.
501 The Surface and ImarisTrack modules were used for object detection and automated tracking

502 of both TEGs (autoregressive motion) and organoids ('connected components' or no tracking).
503 The *Distance Transformation* Xtension was used to measure the distance between TEGs and
504 organoids and thresholds for defining organoid–T cell interactions were visually determined.
505 For tracked TEGs, time-lapse data containing the coordinates of each cell, the values of cell
506 speed, mean square displacement, distance to organoids and dead cell dye channel intensity
507 were exported. For experiments with NCAM1 pre-labelling, the mean intensities of the
508 NCAM1 channel per T cell were exported. For tracked organoids, time-lapse data containing
509 the coordinates of each organoid, the surface area, volume and mean dead cell dye channel
510 intensity were exported.
511
512 **Imaging and sequencing data processing**
513 Analysis of imaging and sequencing data was performed using R Studio version 4.0.2, as well
514 as the following R packages: DESeq2, devtools, dplyr, dtwclust, eulerr, gganimate, ggplot2,
515 ggpubr, ggrepel, gridExtra, hypergeo, kmodR, lme4, lmerTest, MESS, nlme, openxlsx,
516 parallel, patternplot, pheatmap, plotly, plyr, png, purr, RColorBrewer, readxl, reshape2, rgeos,
517 scales, Seurat, sp, spatstat, stats, tidyr, tidyverse, umap, VennDiagram, viridis, xlsx, zoo.
518
519 **PDOs killing dynamics**
520 To quantify cell death dynamics of PDO cultures, > 5000 single organoids were analyzed at
521 each time-point (48 time-points total). The mean dead cell dye intensity within single organoid
522 surfaces, and values were rescaled to a range between 0 and 100 per experiment to normalize
523 for variation in the absolute dead cell dye intensity. Per time point, organoids were classified
524 as 'dying' when the mean dead cell dye intensity was above 7.
525
526 **T cell dynamics analysis and multivariate time series clustering**

527 For the analysis of TEG behavior overtime, the following parameters were used: T cell death,
528 contact with organoids, speed, square displacement and interaction with other T cells.
529 Interactions between TEGs were measured by computing the distance to the nearest neighbor
530 for each cell. To only include active interactions between TEGs that were not engaged to
531 organoids, we considered cells whose mean speed for the last 20 minutes fell within the 3rd
532 quartile. A threshold for interacting T cells was defined as 10 µm between cell centroids and
533 confirmed by visual inspection of imaging data. For each TEG time series, linear interpolation
534 was used to estimate the values in few cases of missing time points. To compare time series
535 independently of their length, cell tracks were cut to a length of 3.3 hrs. For each experimental
536 replicate, the values of each of the numeric variables were converted to z-scores. To enhance
537 the most discrepant values, only the 3rd quartile range values were kept, while the rest was
538 converted to the minimum values. Finally, each numeric variable was scaled to a range between
539 0 and 1 and normalized to the mean of the 0.99 quantile (per experimental replicate). For binary
540 variables (TEG-TEG or TEG-organoid interactions), the values were labelled as 1 or 0 for
541 interaction or no-interaction terms. Similarity between distinct cell tracks was measured using
542 a strategy that allows for best alignment between time-series, previously applied for mitotic
543 kinetics (Cai et al., 2018) or temporal module dynamics comparisons (Schafer et al., 2019). A
544 cross-distance matrix based on the multivariate time-series data was computed using the
545 dynamic time warping algorithm from the package "dtwclust". To visualize distinct cell
546 behaviors in 2 dimensions, dimensionality reduction on the multidimensional feature count
547 table was performed by Uniform Manifold Approximation and Projection method ("umap"
548 package) (Ali et al.; Becht et al., 2018). Clustering was performed using the k-means clustering
549 algorithm with outlier detection. The identity of each cluster was defined by the mean time-
550 series values of the different parameters (speed, square displacement, organoid contact, T cell
551 interactions, cell death) within each cluster (**Figure 2C**). To confirm the identity of each

552 cluster, T cell cluster assignments were back-projected to visualize the surfaces and tracks of
553 particular T cell populations in the imaging dataset (**Figures 2A, S2A and S2B, and S3B**). A
554 combination of datasets with distinct behavioral characteristics was used to construct a global
555 TEG behavior atlas using the described methodology (**Figure 2B**).
556
557 **Cell behavior classification using a Random Forest classifier**
558 For standardized integration of new experiments, we used a random forest classification
559 approach (Breiman, L., 2001) in order to relate cell behavior to the nine behavioral signatures
560 that we found in our global TEG behavior atlas (**Figure 2B**). To allow for inclusion of
561 experiments with a low E:T ratio of 1:25, where the parameter of T cell interaction would be
562 influenced as compared to the standard E:T ratio of 1:3, the following parameters were used:
563 T cell death, organoid contact, speed, square displacement. The reference dataset used to build
564 the global TEG behavior atlas was split into cell tracks to be used as a training dataset (95%)
565 and a test dataset (5%). To reduce dimensionality, for each cell track, four time-series
566 descriptive statistics were quantified and used to train the classifier. For numeric variables, the
567 following measures were computed for each cell track: mean, median, the top 90% of the
568 distribution, and the standard deviation. For binary values, such as the contact with organoids,
569 the mean was calculated, as well as the mean and maximum of cumulative interaction. The
570 random forest classifier was trained using 100 trees on the above-mentioned variables using
571 the nine behavioral signatures as labels (**Figures S2C and S2D**). The test dataset was used to
572 assess for accuracy of the classifier and to determine in which behavioral signatures the errors
573 occurred (**Figure S2E**).
574
575 **Correlation between TEG behavior and organoid killing dynamics**

576 To estimate the correlation between the onset of death in individual organoids and the
577 engagement with T cells belonging to the engaging clusters (C7-9), we implemented a
578 technique of sliding window correlation analysis, previously used for functional brain
579 connectivity (Preti et al., 2017) and genome analysis (Burke et al., 2010). We calculated the
580 Pearson correlation coefficient between the cumulative number of organoid contacts with
581 TEGs from each cluster and the increase in dead cell dye intensity in each over a sliding
582 window of 3 hrs (**Figures 2F and S2F**).
583
584 **T cell serial killing capacity analysis**
585 For accurate long-term (up to 24 h) T cell tracking, TEGs were plated at a E:T ratio of 1:25.
586 Tracks were manually corrected where required. Tracks were divided into shorter subtracks of
587 160 minutes. Using the random forest classifier described above, each subtrack was assigned
588 to a behavioral signature (**Figures S2D and S2E**). The following statistics were calculated for
589 each type of behavioral signature (9 clusters): for continuous variables (square displacement;
590 speed, T cell death) the mean, median and standard deviation of the upper quantile were
591 calculated, and for discrete variables (organoid contact and interaction with T cells) the mean,
592 cumulative mean, maximum and cumulative maximum were calculated. Principal component
593 (PC) analysis was used to reduce the dimensionality. The top 5 PCs were used to classify the
594 change in behavioral signature over time (**Figures S3B and S3C**). Equivalent to the approach
595 that was used for the full tracks in **Figure 2B**, we computed a cross-distance matrix based on
596 the multivariate time-series data using the dynamic time warping algorithm and performed k-
597 means clustering in UMAP space. The change in behavioral signatures was represented in a
598 time-series color plot where each row represents one cell track and the color codes for
599 behavioral signature (**Figure S3C)**. The relative proportion of $CD4^+$ and $CD8^+$ TEGs in each
600 cluster was calculated and plotted next to each long-term classification (**Figure S3C**).

601 TEGs that engaged to organoids were back-projected to the imaging dataset and their
602 first and second actions upon organoid engagement were visually analyzed (**Figure 3D**). TEG
603 morphological plasticity was calculated by measuring the cell elongation (ratio between the
604 longest and shortest axes) per cell and per individual timepoint. For each cell track, the
605 plasticity was then computed as the ratio between the maximal and the minimal cell elongation
606 (**Figure S3F**). The actions of $CD4^+$ and $CD8^+$ TEGs upon organoid engagement (**Figure 3D**)
607 as well as the speed of killing and serial killing potential (**Figures 3G and 3H**) were quantified
608 using Imaris software. Only TEGs were included for which tumor cell killing was clearly
609 observed (usually visible as a decrease in living cell dye and an increase in dead cell dye, which
610 co-occurred in many cases with target cell detachment from the organoid). For cases where a
611 single organoid was fully killed by a single TEG, the number of cells killed by the TEG was
612 calculated by dividing the killed volume by the average volume of a single 13T cell (2182
613 μm^3). The killing rate of TEGs was measured as the time period from target cell engagement
614 until tumor cell death (**Figure 3H**).
615
616 **NCAM1 pre-labelling quantification using 3D imaging data**
617 Behavioral classification of NCAM1 pre-labelled TEGs was performed as described above, by
618 predicting behavioral signatures with the Random Forest classifier. $NCAM1^{+/-}$ TEGs were
619 identified based on an NCAM1 intensity threshold in individual TEGs, visually defined at the
620 timepoints where the 488 nm laser was turned on. To ensure inclusion of true $NCAM1^-$ or
621 $NCAM1^+$ TEGs, two intensity thresholds were defined. Only tracks with a defined $NCAM1^+$
622 or $NCAM1^-$ identity were used for subsequent analysis. For each individual well, a difference
623 in percentage of $NCAM1^+$ and $NCAM1^-$ TEGs was calculated per behavioral signature
624 (**Figures 3L and S3I**).
625

626 **PDO bulk RNA sequencing**

627 For bulk RNA sequencing characterization, RNA of PDOs grown in 'Type 1' culture medium
628 was isolated according to the manufacturer's protocol using the RNeasy Mini Kit (QIAGEN).
629 Quality and quantity of the RNA samples and the libraries were measured with Agilent's
630 Bioanalyzer2100 and Invitrogen™ Qubit™ 3.0 Fluorometer. Quality control was done using
631 FastQC, alignment has been done using STAR
632 (https://github.com/alexdobin/STAR/releases/tag/STAR_2.4.2a) and reads have been mapped
633 to the GRCh37 version of the human reference genome. Quality control on the bams was done
634 using Picard. Read counts were generated with Htseq-count after which normalization is done
635 using DESeq. RPKMs have been calculated with edgeR. For the library preparation the TruSeq
636 Stranded mRNA Library Prep kit from Illumina was used. Sequencing was performed on the
637 nextseq500 sequencer (also Illumina) with single-end 75bp reads. PDO cultures were ranked
638 by responsiveness to TEGs (**Figure 1D**) and differentially expressed genes between the 6 most
639 TEG-sensitive and 6 least TEG-sensitive cultures were analyzed. Genes exhibiting a more than
640 4-fold expression change with an adjusted p-value <0.05 after multiple hypothesis testing
641 correction were used as input gene set enrichment analysis.

642

643 **SORTseq sample preparation**

644 For sequencing of different behavior-enriched TEG populations (**Figure 4A**), TEGs
645 (>0,8x10^6 per condition) were either (1) co-cultured with 13T PDOs (E:T of 1:3) and separated
646 into organoid-engaged (*engaged*) and organoid non-engaged (*non-engaged*) populations by 2
647 slow-spin (30 rcf) centrifugation steps at 6 h co-culture, (2) co-cultured with 10T or 13T PDOs
648 (E:T of 1: 3) and separated at 4 hrs into organoid-engaged and organoid non-engaged
649 populations by a slow-spin (30 rcf) centrifugation step, co-cultured for another 2h with or
650 without addition of fresh PDOs, again followed 2 slow-spin (30 rcf) centrifugation steps to

651 obtain *non-engaged*^{Enriched} and *super-engaged* TEG populations, or (3) cultured for six hrs
652 without addition of PDOs (*no target control*), using 12-wells culture plates (Thermo Fischer)
653 and 'co-culture medium'. To create single-cell suspensions, conditions containing organoids
654 (all '*engaged'* TEG conditions) were treated with TrypLE for seven minutes at 37°C and
655 washed with adDMEM/F12+++. Cells were then stained in FC buffer (2% FCS in
656 PBS) with anti-CD3-APC conjugated antibodies (1:80; BioLegend) and LIVE/DEAD Fixable
657 Near-IR Dead Cell Stain (1:1000; ThermoFisher) for 30 minutes at 4°C and sorted into 384-
658 wells SORTseq plates using a FACS Aria Cell Sorter (BD Biosciences) and directly stored at
659 -80°C until further processing.
660
661 **SORTseq library preparation and sequencing**
662 All sorted plates were processed according to the CEL-Seq2 protocol with the total
663 transcriptome amplification via poly-A RNA-capture, library preparation, and sequencing into
664 Illumina sequencing libraries as previously described(Muraro et al., 2016). Paired-end
665 sequencing (read1: 30 bp; read2: 120 bp) was used to sequence the prepared libraries using an
666 Illumina NextSeq sequencer.
667
668 **Mapping and quantification of SORTseq data**
669 SORTseq data were mapped and reads were counted, using STAR version 2.6.1a on the
670 Hg38p10 human genome (annotated with GenCode v26). Plate-QC was performed using the
671 Sharq pipeline (Candelli et al., 2018). Percentage of ERCC spike-in reads and mitochondrial
672 mRNA reads versus total read count per cell were applied as QC parameters to identify
673 systemic processing or pipetting errors over the plates. Cells with mitochondrial mRNA reads
674 higher than 15%, ribosomal RNA content higher than 30%, or ERCC reads higher than 25%
675 were excluded from the downstream analysis. Cells with fewer than 650 and higher than 4500

676 genes captured, and genes captured in fewer than 2 cells per plate were also excluded. After
677 the initial QC steps, the ERCC spike-in reads were removed from the final count tables.
678
679 **SORTseq and 10x genomics data integration and TEG subpopulation analysis**
680 For analysis of TEGs not exposed to organoids (**Figures 3I, and S3G and S3H**), 3
681 experimental replicates were used consisting of two datasets processed using SORT-seq and
682 one dataset processed using 10x Genomics Chromium Single Cell 3′ gene-expression kit.
683 SORTseq data was processed as described above. For the 10x dataset, (fresh, not co-cultured)
684 TEGs were viability-enriched via FACS by DAPI staining (1:1000; Thermo Fischer) and
685 loaded according to the standard protocol of the Chromium Single Cell 3′ Kit (v3). All the
686 following steps were performed according to the standard manufacturer's protocol. The library
687 was sequenced on an Illumina Novaseq S1-flowcell and 19,000 reads/cell were collected.
688 Single-cell RNAseq data were mapped, and counts of molecules per barcode were quantified
689 using the cellranger(3.1.0) 10x software package to map sequencing data to the GRCh38(3.0.0)
690 reference transcriptome supplied by 10x. Cells with mitochondrial mRNA reads higher than
691 15% and with fewer than 200 or more than 5000 distinct genes were excluded from the
692 downstream analysis. Data were normalized by sequencing depth, scaled to 10,000 counts, log-
693 transformed, and regressed against the UMI-counts and percentage of mitochondrial mRNA
694 using the ScaleData function of the Seurat package. For integration of the 10x genomics (n =
695 1) and SORTseq (n = 2) datasets, we used previously published Seurat v3 data anchor-based
696 integration(Stuart et al., 2019). Briefly, all three datasets were normalized using SCTtransform
697 (Hafemeister and Satija, 2019) followed by selection of 5000 features for downstream
698 integration. Transfer anchors were then learned and applied for integration of all datasets into
699 a combined dataset. Cell visualization and placement in 2D view was achieved using principal
700 component analysis (PCA) followed by Uniform Manifold Approximation and Projection

701 (UMAP)(McInnes et al.). Shared nearest neighbor graph-based clustering was done using
702 Seurat package's FindNeighbors and FindClusters functions with a resolution of 0.8. For cell
703 type identification marker genes for each cluster were calculated using the FindAllMarkers
704 function and examined to profile marker genes that correspond to known cell types. Additional
705 support for identifying cell subpopulations similitudes was achieved by analyzing the
706 differentially expressed genes with a cell-type annotation tool(Cao et al.). Main marker genes
707 used for TEG subpopulations identification are plotted in **Figure S3H.**
708
709 **Pseudotime Trajectory Inference**
710 Two experimental SORTseq replicates of TEGs co-cultured with 13T PDOs, generated as
711 described above, were used for trajectory interference (**Figure S4B)**. Proliferating T cells were
712 excluded from the analysis since they did not show any dynamic inflammatory genes during
713 the analysis. Afterwards, the gene expression table was log normalized with 10,000 scaling
714 factor. Cell visualization and placement in 2D view was achieved using principal component
715 analysis (PCA) followed by Uniform Manifold Approximation and Projection (UMAP)
716 (McInnes et al., 2020). Shared nearest neighbor graph-based clustering was done using Seurat
717 package's FindNeighbors and FindClusters functions with the resolution of 2. Based on marker
718 gene expression of CD8, CD4 and IL17RB (Terrier et al., 2010), TEGs were sub-clustered into
719 3 subtypes; $IL17RB^{-}CD8^{+eff}$, $IL17RB^{-}CD4^{+eff}$ and $IL17RB^{+}CD4^{+mem}$. Downstream analyses
720 were done on each subset separately and compared with each other where mentioned.
721 RunFastMNN function from SeuratWrappers package was utilized to correct for batch effects
722 between the two SORTseq replicates. Unless specified, batch corrected UMAP values were
723 used for visualization of single cells. We used Monocle3 (Cao et al., 2020) package to infer the
724 pseudotime trajectory and significantly dynamic genes for each T cell subtype. For each cell
725 subtype either *no target control* or *non-engaged*^{Enriched} TEGs were designated as the root of the

726 trajectory. In order to have comparable results from both Seurat and Monocle3 packages, the
727 FastMNN batch corrected UMAP coordinates were imported and used throughout the
728 trajectory analysis in Monocle3. In IL17RB^{-}CD4^{+eff} and IL17RB^{+}CD4^{+mem} subtypes, Monocle
729 identified *no target control* cells as a separate partition. In order to have all cells along with a
730 single pseudotime spectrum (e.g., not having several cells with a same pseudotime value), we
731 added maximum pseudotime values of *no target control* T cells to pseudotime values of
732 remaining cells in that subtype. For all TEG subtypes, significant dynamic genes along with
733 the pseudotime trajectory were calculated and identified using Monocle3's graph_test function
734 using 1e-20 *q* value as the significance cutoff. Afterwards, using k-means clustering and also
735 visual inspection of the genes' behavior over the pseudotime, TEGs were clustered into sub-
736 clusters with similar pattern (CL1-8; **Figure 4G**). The expression profile of the genes along
737 with the pseudotime trajectory was plotted using pheatmap package(Kolde et al.) using row
738 scaled (z-score) expression values. Smoothed gene(s) behavior was calculated and visualized
739 recruiting gam smoothing function in ggplot2 package (Wilkinson, 2011).
740
741 **Behavior signature inference over the pseudotime.**
742 To align the pseudotime inference with the different behavioral signatures that we identified
743 with BEHAV3D, we build a probability map distribution for different behavioral signatures
744 over the pseudotime, based on the fundamental principle of transitivity of probabilistic
745 distribution (**Figure 4F**). We defined three states of cells quantified by different methods:
746 • Behavioral_signatures (B_{sig}): {*Static, Lazy, Medium-scanner, Scanner, Super scanner,*
747 *Tickler, Engager, Super engager*}. Behavioral signatures of cells identified by imaging
748 (**Figure 4B**).

749 • Experimental_engagement_state (Exp_{eng}): {*No target control, Non-engaged, Non-*
750 *engaged*^{enriched}*, Engaged, Super-engaged*}. Cell distribution among different
751 experimental conditions (**Figure 4A**)
752 • UMAP_cluster (U_{cl}): {1…X}. Cell assignment to distinct clusters grouping cells with
753 similar gene expression. Shared nearest neighbor graph-based clustering was repeated
754 several times using Seurat package's FindNeighbors and FindClusters functions with a
755 resolution ranging from 1 to 7.
756 From these three different cell states, the following information was quantified:
757 • p(B_{sig}|Exp_{eng}): For each Experimental_engagement_state we quantified the probability
758 distribution of each Behavioral_signature (**Figure 4F**. This was achieved by
759 reproducing the Experimental_engagement_states *in silico* on our imaging data. These
760 values were calculated separately for $CD4^+$ and $CD8^+$ TEGs.
761 • p(Exp_{eng}|U_{cl}): For each UMAP_cluster, we quantified the probability of each
762 Experimental_engagement_state to belong to this cluster.
763 Given these probabilities, we then quantified for each T cell the probability distribution of each
764 unique Behavioral_signature in each UMAP_cluster, using the equation:
765
766 As a result, each cell was assigned a certain probability distribution for different behavioral
767 signatures. To refine the probability map, the same process was repeated for 7 runs with
768 different cluster sizes and the final probability distributions were averaged per cell. Note that
769 for cells belonging to the *No target control* Experimental_engagement_state, a
770 Behavioral_signature called *No target control* was assumed. The probability distribution along
771 the pseudotime trajectory was plotted using pheatmap package[70] of scaled values for each
772 behavioral signature. Given that the non-engaged behavioral signatures (*Static, Lazy, Slow*
773 *scanner, Medium scanner, Super scanner*) exhibited an identical probability map, their values

774 were plotted together. For visualization purpose, extreme outlier values of skewed distributions
775 were transformed to a maximal cutoff value. Based on the probability distribution of different
776 behavioral signatures, the pseudotime was divided into 4 stages (Baseline (no organoids);
777 Environmental stimuli, Short engagement, Prolonged engagement) for each TEG subtype
778 ($CD8^{+eff}$, $CD4^{+eff}$ and $CD4^{+mem}$).
779
780 **Differential gene expression analysis of TEGs co-cultured with distinct PDO cultures**
781 For comparison of TEGs targeting 10T or 13T PDOs (**Figures 5A-5C**), SORTseq dataset was
782 used including TEGs from distinct Experimental engagement states: *Non-engaged*^{Enriched} and
783 *super engager*. *No target control* TEGs were used as a control group. SORTseq data were
784 mapped and quantified and visualized with UMAP as described above. Differential gene
785 expression analysis was performed with the FindMarkers function from Seurat v3. Common
786 and specific gene sets were filtered and visualized by Venn diagram with the VennDiagram
787 package.
788
789 **Gene set enrichment analysis**
790 The functional enrichment analysis in this study for pathway and biological processes
791 annotations for gene sets of interest was conducted using ToppFun on the ToppGene
792 Suite(Kaimal et al.) (**Figures 1H, S4C, and S5B**). An enrichment score was assigned based on
793 gene enrichment ratio and log p value. For redundant annotations, the annotation with the
794 highest gene enrichment ratio was selected. The pathways and biological processes with
795 highest enrichment for gene set of interest were displayed in RStudio.
796
797 **Serial killer gene signature analysis**

798 Genes of CL7 (**Figure 4G; Table S4 and S5**) were analysed to identify a unique signature for
799 killer TEGs. 61/83 genes composing this cluster were common to TEGs incubated with 13T
800 and 10T organoids and underwent extensive literature curation to identify genes with a known
801 role in T cell cytotoxicity; T cell biology (not related to cytotoxicity); morphological plasticity
802 or other processes such as GTPase signaling, ribogenesis and transcriptional regulation.
803 Overlapping gene roles were plotted in a Venn diagram with the Venneuler package (**Figure**
804 **4K**).
805
806 **Statistical analysis**
807 Statistical analysis was performed using R or Prism 7 software (GraphPad). Results are
808 represented as mean ± s.e.m. unless indicated otherwise; *n* represents independent biological
809 replicates. Two-tailed unpaired t-tests were performed between two groups, unless indicated
810 otherwise. Pearson correlation was used for paired comparison between three different readouts
811 (IFN-γ production, cell viability and live imaging). For live-cell imaging, the increase in dead
812 cell dye between the first and last time point was used as measure. To compare tumor volume
813 in mice treated with TEGs or TEG001 mock cells, two-way ANOVA with repeated measures
814 was performed. To compare frequencies of different behavioral signatures between PDOs, a
815 Pearson's Chi-squared test was applied. To compare the percentage of dead organoids when
816 TEGs were co-cultured with different PDOs, a one-way ANOVA followed by Bonferroni
817 correction was performed. To estimate the change in correlation between 13T PDO death
818 dynamics and cumulative contact with TEGs for different behavioral signatures, data was fitted
819 to a linear mixed model with experimental replicate as random effect to account for variation
820 between them. For cell type enrichment analysis of TEGs' first and second action after
821 engagement, a hypergeometric test was used (Fisher exact test). For comparisons of
822 percentages of distinct TEG subtypes in the same well ($CD4^+$ vs $CD8^+$ or $NCAM^+$ vs NCAM),

823 for each behavioral signature data were fitted to a linear regression model with each individual
824 replicate set as random effect to account for variation between them. For each fitted model, an
825 analysis of variance was computed with an F-test. For comparison of IFN-β treatment, paired
826 t test was performed.
827
828 **Data availability**
829 RNA sequencing data of this study have been deposited in the Gene Expression Omnibus
830 (GEO), under accession number GSE172325 (secure token qfahqkgsjnwplgh). Imaging data is
831 available upon request.
832
833 **Code availability**
834 Upon request.
835
836 **Acknowledgements**
837 We are grateful for the technical support from the Princess Máxima Center for Pediatric
838 Oncology and the Hubrecht Institute and Zeiss for imaging support and collaborations. All the
839 imaging was performed at the Princess Máxima Imaging Center. We thank the Princess
840 Máxima Center Organoid Facility for organoid culture support, the flow cytometry facilities at
841 the Princess Máxima Center and Laboratory of Translational Immunology (University Medical
842 Center Utrecht) for cell sorting, the Princess Máxima Center Single Cell Genomics Facility for
843 help with scRNAseq analysis, Single Cell Discoveries (https://www.scdiscoveries.com) for
844 library preparations, and the Hartwig Medical Foundation
845 (https://www.hartwigmedicalfoundation.nl/) for the sequencing. We also acknowledge the
846 Hubrecht Organoid Technology (HUB) for providing PDOs, QVQ for providing NCAM1
847 nanobodies. We would like to thank Linde Meyaard, Jeffrey Beekman and the Dream3D^{LAB} for

848 providing feedback on the manuscript, and Alberto Miranda-Bedate for pilot PDO sequencing
849 analysis, Hannah Johnson for the voice over of the video and Anna Allemany for insightful
850 advice for behavioral-transcriptomics inference. This work was financially supported by the
851 Princess Máxima Center for Pediatric Oncology, Grants ZonMW 43400003, VIDI ZonMW
852 917.11.337, CRUK OPTIMISTICC C10674/A27140 (J.P., H.C), Netherlands Organ-on-Chip
853 Initiative NWO 024.003.001 (J.P., H.C.), KWF Grants UU 2014-6790, UU 2015-7601, and
854 UU 2019-12586 (J.K); Grant UU 2017-11393 (Z.S and J.K). K.K. was the recipient of a VENI
855 grant from the Netherlands Organization for Scientific Research (NWO-
856 ZonMW,016.166.140) and was a long-term fellow of the Human Frontier Science Program
857 Organization (HFSPO, LT771/2015). A.C.R is supported by an ERC-starting grant 2018
858 project 804412. J.F.D was supported by a Marie Curie Global Fellowship and a VENI grant
859 from the Netherlands Organization for Scientific Research (NWO).
860

861 **Author contributions**

862 J.F.D grew organoids and performed imaging experiments with assistance from H.G.R., E.J.V.
863 and M.G. M.A. designed and performed the computational analysis. M.A. and J.F.D. analyzed
864 the data. M.B.B. and M.B.R. assisted with imaging data processing. J.F.D., A.K.L.W. and E.K.
865 performed scRNAseq experiments. J.P. and D.F. processed PDO sequencing data. H.C.R.A.
866 performed NCAM1 sorts. F.K. and P.B. analyzed the scRNAseq data. A.C. and E.K. produced
867 TEGs and performed IFN-γ assays. H.G.R., I.J. and A.D.M. performed *in vivo* experiments.
868 A.M.B assisted with computational analysis. R.L.I and M.B.R. made the video. O.K. provided
869 organoid cultures. Y.B.E. and K.K. provided support and developed the co-culture live cell
870 staining protocol that was used and further adapted. J.F.D, M.A. and A.C.R. designed the study
871 and wrote the manuscript with support from A.M.M.E., E.J.W., H.G.S, Z.S., J.K. and H.C.
872 This work was jointly supervised by A.C.R, Z.S, J.K, H.C who share senior authorship.

873

874 **Declaration of Interests**

875 H.C., Y.B.E. and K.K. are named as inventors on patents or patents pending on Lgr5-stem cell
876 based organoid technology and immune cell organoid co-cultures. For full disclosure of HC:
877 https://www.uu.nl/staff/JCClevers/Additional%20functions. J.F.D. is named as inventor on a
878 patent related to organoid technology. Z. S. and J.K are inventors on different patents with γδ
879 TCR sequences, recognition mechanisms, and isolation strategies. J.K. receives research
880 funding from and is scientific advisor and shareholder of Gadeta (www.gadeta.nl).

881

882 **Figure legends**

883

884 **Figure 1. TEG efficacy across organoids of multiple breast cancer subtypes detected by**
885 **multispectral 3D live imaging and *in vivo* TEG targeting**. (**A**) Schematic representation of
886 co-culture preparation. TEGs were generated by engineering peripheral blood αβ T cells to
887 express a defined Vγ9/Vδ2 TCR via retroviral transduction. TEGs were then co-cultured with
888 patient-derived breast organoids (PDOs). (**B**) Schematic representation of the BEHAV3D
889 platform. Fluorescent dyes were combined to specifically label organoids (yellow), TEGs
890 (blue) and dead cells (red). Co-cultures of organoids and TEGs were imaged in 96-well plates
891 using spectral confocal microscopy in 3D, followed by segmentation and tracking of organoids
892 and T cells, and subsequent behavior classification. TEGs of experimental conditions as
893 indicated were sequenced and pseudotime ordering was used to integrate behavioral data.
894 Identified targets were used to manipulate TEG targeting. (**C**) Representative 3D multispectral
895 images of breast PDO cultures (yellow) that show low (1837M), intermediate (10T) and high
896 (13T) killing by TEGs (blue) at the indicated time points of imaging. Dead cells depicted in
897 red. Scale bars, 100 µm (left two columns) and 30 µm (right two columns). (**D**) Quantification
898 of killing of organoids derived from 14 different BC patients upon 24 hr co-culture with TEGs
899 by 3D live cell imaging. All data were corrected for control LM1 T cell responses. (n = 4
900 independent experiments; mean ± s.e.m.; TNBC = triple negative breast cancer; ER = estrogen
901 receptor; PR = progesterone receptor). (**E**) Representative 3D multispectral images showing
902 automated rendering of single organoids (confetti colors) and T cells (blue) (left image), and
903 an enlarged section showing presence of dead cell dye (red) in a single organoid (transparent
904 purple rendering) and TEGs (transparent blue rendering) at the indicated time of co-culture.
905 Scale bars, 100 µm (left image) and 30 µm (right image). (**F**) Quantification of the percentage
906 of dying single organoids (% of total) over time for each PDO co-cultured with TEGs (n = 4

907 independent experiments; mean ± s.e.m.). (**G**) Quantification of the volume of tumors overtime
908 generated by subcutaneous transplantation of 13T (black lines) or 169M organoids (orange
909 lines). Animals received 2 injections of either TEGs (dashed line) or control TEG011 cells
910 (Control; solid line) at the indicated timepoints. (n ≥5 per condition; mean ± s.e.m.). Statistical
911 analysis was performed by Two-Way ANOVA with repeated measures: 13T-TEG vs 13T-
912 control $p < 0.0001$; 169M-TEG vs 169M-control $p=0.0016$. (**H**) Gene ontology enrichment
913 analysis of differentially expressed genes between the six highest versus six lowest TEG-
914 sensitive organoid cultures from d.
915
916 **Figure 2. TEGs exposed to PDOs display high diversities in their behavior with distinct**
917 **killing potential.** (**A**) Representative image of automated tracking of each TEG (left image;
918 10 hrs tracks are rainbow-colored for time). Tracks were classified according to TEG behavior
919 and back-projected in the image (right image; color-coded by cluster). Scale bars, 50 µm. (**B**)
920 Umap plot showing nine color-coded clusters identified by unbiased multivariate timeseries
921 dynamic time warping analysis. Each data point represents a T cell track of 3.3 hrs. Numbers
922 refer to cluster names presented in (C). (**C**) Heatmap depicting relative values of T cell features
923 indicated for each cluster, named according to their most distinct characteristics. AU: arbitrary
924 units in respect to maximal and minimal values for each feature. (OC, organoid contact; Dis,
925 square displacement; Sp, speed; TI, T cell interactions; CD, cell death) (**D**) 3D-rendered images
926 of 100T (low-targeting; left image) and 13T (high-targeting; right image) organoids (grey) and
927 TEGs with 3.3 hr tracks belonging to *lazy* (green) and *super engager* (red) clusters. Scale bars,
928 20 µm. (**E**) Behavioral cluster distribution of TEGs co-cultured with the indicated PDOs and a
929 normal organoid culture (left plot), in relation to their killing capacity (right bar graph)
930 represented as the percentage of dying organoids (% of total) (n ≥ 3 independent experiments;
931 mean ± s.e.m.). X^2 test; $p = 1.132e-08$. (**F**) Pearson correlation between behavior cluster size

932 and the percentage of dying organoids represented in d. CL9 p=0.00006; CL8 p= 0.009; CL7
933 p=0.006; CL5 p=0.014; CL4 p=0.022; CL2 p=0.0019. (n ≥ 3 independent experiments; mean).
934 (**G**) Change in correlation between 13T organoid death dynamics (measured as increase in dead
935 cell dye) and cumulative contact with TEGs (from cluster (C)7-9). Data is represented as mean
936 correlation per timepoint of all single organoids (n = 4 independent experiments). Linear mixed
937 model fitting with each experimental replicate as a random effect: C9 vs C8 p= 5.19e-06; C9
938 vs C7 p < 2e-16.
939
940 **Figure 3. Unique targeting features of TEGs subpopulations and serial killer potential**.
941 (**A**) Representative 3D-rendered images of $CD4^+$ (blue) and $CD8^+$ (red) TEGs and their full
942 tracks (up to 10 hrs) co-cultured with the 13T organoids (grey surface rendering at t = 0).
943 Overview: Scale bar, 50 µm. Zoomed images: Scale bar, 30 µm (**B**) Relative behavioral cluster
944 distribution of TEGs co-cultured with the indicated PDOs and a normal organoid culture. (**C**)
945 Behavioral cluster size difference (%) between $CD4^+$ and $CD8^+$ TEGs co-cultured with the
946 indicated PDOs and a normal organoid culture calculated from B. (n ≥ 3 independent
947 experiments for each co-culture; mean ± s.e.m.) Linear regression model fitting with each well
948 as a random effect: C9 p=7.52E-06; C8 p=0.0034; C7 p=0.00018; C6 p=0.000023; C5
949 p=0.0062; C4 p=0.01; C3 p= 0.001; C1 p=3.01E-06. (**D**) Quantification of the first action and
950 second action of $CD4^+$ and $CD8^+$ TEGs after they engaged with an organoid. n = 3 replicates.
951 Hypergeometric test was used to analyze cell type enrichment in each category. "Kills multiple
952 cells" p<0.0001; "Kills one cell" p= 0.000015; "No killing" p= 0.0018. (**E**) 3D multispectral
953 images showing a $CD4^+$ TEG (green) that kills a 13T tumor cell (becomes red) in a first
954 organoid (yellow) and a second tumor cell in a neighboring organoid (upper panel), and a $CD8^+$
955 TEG (blue) killing a complete 13T organoid of ~18 cells (yellow becoming red) in 11 hrs
956 (lower panel). Scale bars, 30 µm. (**F**) Processed images of j showing 3D-rendered organoids

957 (grey) at t = 0 and the $CD4^+$ TEG (green) or the $CD8^+$ TEG (blue) with their full track rainbow-
958 colored for time. Scale bars, 10 µm. (**G**) Quantification of the number of cells killed in a
959 sequence by $CD8^+$ TEGs in time. (n = 3 independent experiments). (**H**) Quantification of the
960 time it takes to kill one 13T tumor cell for $CD4^+$ TEGs and $CD8^+$ TEGs (n = 3 independent
961 experiments). (**I**) UMAP embedding showing the expression levels of NCAM1. Color gradient
962 represents the log_2-transformed normalized counts of genes. (**J**) Quantification of the
963 percentage of dying 13T organoids (% of total) at 10 hrs of co-culture with either sorted
964 $NCAM1^-CD8^+$ TEGs or $NCAM1^+CD8^+$ TEGs (n = 5 independent experiments; mean ± s.e.m.).
965 Two-tailed unpaired t test, p= 0.0001036. (**K**) Schematic representation of fluorescent labeling
966 strategy of $CD8^+$ TEGs with NCAM1 nanobody and efluor-450 to image and track NCAM1-
967 positive versus -negative TEGs. (**L**) Behavioral cluster difference (%) between $NCAM1^-CD8^+$
968 TEGs or $NCAM1^+CD8^+$ TEGs co-cultured with 13T organoids. (n = 6 independent
969 experiments; mean ± s.e.m.). Linear regression model fitting with each experimental replicate
970 as a random effect: CL9 p=0.0002; CL8 p=0.07; CL2 p=0.005; CL1 p=0.02. (**M**) 3D-rendered
971 images of 13T organoids (grey) from the same well with NCAM+ 'super-engager' CD8+ TEGs
972 (top image) and NCAM- 'lazy' and 'dying' CD8+ TEGs (bottom image). Scale bars, 10 µm.
973

974 **Figure 4. Behavioral-transcriptomic profiling of TEGs upon PDO exposure, engagement**
975 **and killing.** (**A**) Schematic representation of cell population separation for isolation and
976 sequencing of *super-engaged*, *engaged*, *non-engaged*; *non-engaged*^{Enriched}, and *no target*
977 *control* TEGs. (**B**) Distribution of the 9 behavioral signatures described in **Figures 2B and 2C**
978 of the indicated behavior-enriched TEG populations isolated at 6 hrs of co-culture. (**C-E**)
979 UMAP embedding of pooled scRNAseq profiles showing distribution of, $CD8^{+eff}$, $CD4^{+eff}$,
980 $CD4^{+mem}$ TEGs (C), the 5 behavior-enriched TEG populations described in a (D), and
981 normalized gene expression of IFNG and GZMB (E). Colors represent the log_2-transformed

982 normalized counts of genes. (**F**) Heatmap representing the probability distribution of different
983 behavioral signatures and *no target control* over pseudotime for $CD8^{+eff}$, $CD4^{+eff}$ and $CD4^{+mem}$
984 TEGs. Color represents the scaled probability for each behavioral group. (**G**) Heatmap
985 showing normalized gene expression dynamics of TEGs upon exposure and engagement to
986 13T PDOs. Columns represent T cells ordered in pseudotime, rows represent the expression of
987 genes, grouped based on similarity, resulting in 8 gene clusters (CL). CL1-3 represent gene
988 expression patterns shared among TEG subsets. CL4-8 show different expression dynamics
989 between TEG subsets. Horizontal color-bar (on top) represents the corresponding stage of
990 targeting based on data in f. (**H**) Averaged gene expression over pseudotime for all genes from
991 indicated GO terms for the indicated TEG subtypes. Graph background color-shading represent
992 the corresponding stage of targeting. Line colors indicate GO term. (**I**) Gene-expression dot
993 plot for a curated subset of genes at different stages of targeting. Rows depict genes. Dot color
994 gradient indicates average expression, while size reflects the proportion of cells expressing a
995 particular gene (%). (**J**) Violin plots for different TEG subtypes showing averaged expression
996 of genes related to GO term 'Regulation of cell killing' enriched in CL7 from g. Colors indicate
997 different stages of targeting. (**K**) Venn diagram depicting common and unique functions from
998 61 conserved genes composing a (serial) killer gene signature.
999
1000 **Figure 5. IFN-I signaling in PDOs primes TEG efficacy.** (**A**) Top panel: UMAP embedding
1001 of pooled scRNA-seq profiles from *super-engaged* and *non-engaged*^{Enriched} TEG populations
1002 co-cultured with either 13T or 10T PDOs; and *no target control* T cells. TEGs are colored per
1003 experimental condition. Bottom panel: UMAP plot showing the expression levels of IFNG and
1004 GZMB. Colors represent the log_2-transformed normalized counts of genes. (**B**) Venn diagrams
1005 depicting common and unique genes upregulated in TEGs upon 13T and 10T organoid
1006 exposure (environmental stimuli; top panel) or prolonged engagement (*super engagers*; bottom

1007 panel). (**C**) Heatmap of gene expression for genes involved in functional annotations of interest
1008 ("Response to IFN-I", "Cytokine response"), grouped according to TEG populations. (**D**)
1009 IFNA and IFNB expression in PDOs from the BC panel in **Figure 1D**. (**E-G**) Quantification
1010 of dying single organoids in presence or absence of recombinant IFN-β for the following
1011 conditions: organoids co-cultured with TEGs with direct addition of IFN-β, corrected for
1012 responses of LM1 control T cells (E); organoids pre-incubated with IFN-β for 24 hrs before
1013 co-culture with TEGs, corrected for responses of LM1 control T cells (F), and organoids pre-
1014 incubated with IFN-β for 24 hrs and cultured in absence of TEGs (G). Lines connect
1015 experimental replicates. ($n \geq 3$). Statistical analysis in (F) was performed by paired t test: 34T-
1016 IFN-β vs 34T-control $p < 0.0006$; 27T-IFN-β vs 27T-control $p < 0.0216$; 10T-IFN-β vs 10T-
1017 control $p < 0.0402$.
1018

1019 **References**

1020 Abbas, A., et al. (2020). The activation trajectory of plasmacytoid dendritic cells in vivo during
1021 a viral infection. Nature Immunology *21*, 983–997.

1022 Ali, M., Jones, M.W., Xie, X. et al. (2019). TimeCluster: dimension reduction applied to
1023 temporal data for visual analytics. Vis Comput *35*, 1013–1026.

1024 Asmal, M., Colgan, J., Naef, F., Yu, B., Lee, Y., Magnasco, M., and Luban, J. (2003).
1025 Production of ribosome components in effector CD4+ T cells is accelerated by TCR
1026 stimulation and coordinated by ERK-MAPK. Immunity *19*, 535–548.

1027 Bar-Ephraim, Y.E., Kretzschmar, K., and Clevers, H. (2019). Organoids in immunological
1028 research. Nat Rev Immunol *28*, 514.

1029 Barnes, S.E., Wang, Y., Chen, L., Molinero, L.L., Gajewski, T.F., Evaristo, C., and Alegre,
1030 M.-L. (2015). T cell-NF-κB activation is required for tumor control in vivo. J Immunother
1031 Cancer *3*, 1.

1032 Becht, E., McInnes, L., Healy, J., Dutertre, C.-A., Kwok, I.W.H., Ng, L.G., Ginhoux, F., and
1033 Newell, E.W. (2019). Dimensionality reduction for visualizing single-cell data using UMAP.
1034 Nat. Biotechnol *37*, 34-44.

1035 Benci, J.L., Xu, B., Qiu, Y., Wu, T.J., Dada, H., Twyman-Saint Victor, C., Cucolo, L., Lee,
1036 D.S.M., Pauken, K.E., Huang, A.C., et al. (2016). Tumor Interferon Signaling Regulates a
1037 Multigenic Resistance Program to Immune Checkpoint Blockade. Cell *167*, 1540–1554.e12.

1038 Borden, E.C. (2019). Interferons α and β in cancer: therapeutic opportunities from new insights.
1039 Nat Rev Drug Discov *18*, 219–234.

1040 Boukhaled, G.M., Harding, S., and Brooks, D.G. (2021). Opposing Roles of Type I Interferons
1041 in Cancer Immunity. Annu Rev Pathol *16*, 167–198.

1042 Breiman, L. (2001). Random Forests. Machine Learning *45*, 5–32.

1043 Broutier, L., Andersson-Rolf, A., Hindley, C.J., Boj, S.F., Clevers, H., Koo, B.-K., and Huch,
1044 M. (2016). Culture and establishment of self-renewing human and mouse adult liver and
1045 pancreas 3D organoids and their genetic manipulation. Nat Protoc *11*, 1724–1743.

1046 Burke, M.K., Dunham, J.P., Shahrestani, P., Thornton, K.R., Rose, M.R., Long A.D. (2010)
1047 Genome-wide analysis of a long-term evolution experiment with Drosophila. Nature *467*, 587-
1048 90.

1049 Cai, Y., Hossain, M.J., Hériché, J.-K., Politi, A.Z., Walther, N., Koch, B., Wachsmuth, M.,
1050 Nijmeijer, B., Kueblbeck, M., Martinic-Kavur, M., et al. (2018). Experimental and

1051 computational framework for a dynamic protein atlas of human cell division. Nature *561*, 411–
1052 415.

1053 Candelli, T. et al. (2018) Sharq, a versatile preprocessing and QC pipeline for Single Cell RNA-
1054 seq. BioRxiv 250811

1055 Cao, J., Spielmann, M., Qiu, X. et al. (2019). The single-cell transcriptional landscape of
1056 mammalian organogenesis. Nature *566*, 469-502.

1057 Cao, Y. et al. (2020) SCSA: a cell type annotation tool for single-cell RNA-seq data. Frontiers
1058 in Genetics *11*, 490.

1059 Cattaneo, C.M., Dijkstra, K.K., Fanchi, L.F., Kelderman, S., Kaing, S., van Rooij, N., Van den
1060 Brink, S., Schumacher, T.N., and Voest, E.E. (2020). Tumor organoid-T-cell coculture
1061 systems. Nat Protoc *15*, 15–39.

1062 Cazaux, M., Grandjean, C.L., Lemaître, F., Garcia, Z., Beck, R.J., Milo, I., Postat, J., Beltman,
1063 J.B., Cheadle, E.J., and Bousso, P. (2019). Single-cell imaging of CAR T cell activity in vivo
1064 reveals extensive functional and anatomical heterogeneity. J. Exp. Med. *216*, 1038–1049.

1065 Chen, D.S., and Mellman, I. (2017). Elements of cancer immunity and the cancer-immune set
1066 point. Nature *541*, 321–330.

1067 Collins, S., Wolfraim, L.A., Drake, C.G., Horton, M.R., and Powell, J.D. (2006). Cutting Edge:
1068 TCR-induced NAB2 enhances T cell function by coactivating IL-2 transcription. The Journal
1069 of Immunology *177*, 8301–8305.

1070 Crowther, M.D., et al. (2020). Genome-wide CRISPR-Cas9 screening reveals ubiquitous T cell
1071 cancer targeting via the monomorphic MHC class I-related protein MR1. Nature Immunology
1072 *21*, 178–185.

1073 Dekkers, J.F., et al. (2019). High-resolution 3D imaging of fixed and cleared organoids. Nat
1074 Protoc *14*, 1756–1771.

1075 Dekkers, J.F., et al. (2021). Long-term culture, genetic manipulation and xenotransplantation
1076 of human normal and breast cancer organoids. Nat Protoc *16*, 1936-1965.

1077 Dijkstra K.K. et al. (2018). Generation of Tumor-Reactive T Cells by Co-culture of Peripheral
1078 Blood Lymphocytes and Tumor Organoids. Cell *174*, 1586–1598.e12.

1079 Dunn, G.P., et al. (2005). A critical function for type I interferons in cancer immunoediting.
1080 Nature Immunology *6*, 722–729.

1081 Esteva, F.J., Hubbard-Lucey, V.M., Tang, J., and Pusztai, L. (2019). Immunotherapy and
1082 targeted therapy combinations in metastatic breast cancer. Lancet Oncol. *20*, e175–e186.

1083 Ganesh, K., Wu, C., O'Rourke, K.P., Szeglin, B.C., Zheng, Y., Sauvé, C.-E.G., Adileh, M.,
1084 Wasserman, I., Marco, M.R., Kim, A.S., et al. (2019). A rectal cancer organoid platform to
1085 study individual responses to chemoradiation. Nat. Med. *25*, 1607–1614.

1086 Gründer, C., van Dorp, S., Hol, S., Drent, E., Straetemans, T., Heijhuurs, S., Scholten, K.,
1087 Scheper, W., Sebestyen, Z., Martens, A., et al. (2012). γ9 and δ2CDR3 domains regulate
1088 functional avidity of T cells harboring γ9δ2TCRs. Blood *120*, 5153–5162.

1089 Hafemeister, C., and Satija, R. (2019). Normalization and variance stabilization of single-cell
1090 RNA-seq data using regularized negative binomial regression. Genome Biol. *20*, 296.

1091 Halle, S., Keyser, K.A., Stahl, F.R., Busche, A., Marquardt, A., Zheng, X., Galla, M.,
1092 Heissmeyer, V., Heller, K., Boelter, J., et al. (2016). In Vivo Killing Capacity of Cytotoxic T
1093 Cells Is Limited and Involves Dynamic Interactions and T Cell Cooperativity. Immunity *44*,
1094 233–245.

1095 Jacob, F., Salinas, R.D., Zhang, D.Y., Nguyen, P.T.T., Schnoll, J.G., Wong, S.Z.H., Thokala,
1096 R., Sheikh, S., Saxena, D., Prokop, S., et al. (2020). A Patient-Derived Glioblastoma Organoid
1097 Model and Biobank Recapitulates Inter- and Intra-tumoral Heterogeneity. Cell *180*, 188–
1098 204.e22.

1099 Jacquelot, N., Yamazaki, T., Roberti, M.P., Duong, C.P.M., Andrews, M.C., Verlingue, L.,
1100 Ferrere, G., Becharef, S., Vétizou, M., Daillère, R., et al. (2019). Sustained Type I interferon
1101 signaling as a mechanism of resistance to PD-1 blockade. Cell Res *29*, 846–861.

1102 Johanna, I., Straetemans, T., Heijhuurs, S., Aarts-Riemens, T., Norell, H., Bongiovanni, L., de
1103 Bruin, A., Sebestyen, Z., and Kuball, J. (2019). Evaluating in vivo efficacy - toxicity profile of
1104 TEG001 in humanized mice xenografts against primary human AML disease and healthy
1105 hematopoietic cells. J Immunother Cancer *7*, 69.

1106 June, C.H., and Sadelain, M. (2018). Chimeric Antigen Receptor Therapy. N Engl J Med *379*,
1107 64–73.

1108 Kaimal V, Bardes EE, Tabar SC, Jegga AG, Aronow BJ. (2010). ToppCluster: a multiple gene
1109 list feature analyzer for comparative enrichment clustering and network-based dissection of
1110 biological systems. Nucleic Acids Res, *38* (Web Server issue):W96-W102.

1111 Kierkels, G.J.J., Scheper, W., Meringa, A.D., Johanna, I., Beringer, D.X., Janssen, A.,
1112 Schiffler, M., Aarts-Riemens, T., Kramer, L., Straetemans, T., et al. (2019). Identification of a
1113 tumor-specific allo-HLA-restricted γδTCR. Blood Adv *3*, 2870–2882.

1114 Kolde, R., et al. (2015). Package "pheatmap." Mran.Microsoft.com

1115 Liu, H., Rhodes, M., Wiest, D.L., and Vignali, D.A. (2000). On the dynamics of TCR:CD3
1116 complex cell surface expression and downmodulation. Immunity *13*, 665–675.

1117 Lukonin, I., Serra, D., Meylan, L.C., Volkmann, K., Baaten, J., Zhao, R., Meeusen, S., Colman,
1118 K., Maurer, F., Stadler, M.B., et al. (2020). Phenotypic landscape of intestinal organoid
1119 regeneration. Nature *586*, 275–280.

1120 Marcu-Malina, V., Heijhuurs, S., van Buuren, M., Hartkamp, L., Strand, S., Sebestyen, Z.,
1121 Scholten, K., Martens, A., and Kuball, J. (2011). Redirecting αβ T cells against cancer cells by
1122 transfer of a broadly tumor-reactive γδT-cell receptor. Blood *118*, 50–59.

1123 McInnes, L., Healy, J., Melville J. (2020) Umap: Uniform manifold approximation and
1124 projection for dimension reduction. ArXiv 1802.03426

1125 Muraro, M.J., Dharmadhikari, G., Grün, D., Groen, N., Dielen, T., Jansen, E., van Gurp, L.,
1126 Engelse, M.A., Carlotti, F., de Koning, E.J.P., et al. (2016). A Single-Cell Transcriptome Atlas
1127 of the Human Pancreas. Cell Syst *3*, 385–394.e3.

1128 Neal, J.T., et al. (2018). Organoid Modeling of the Tumor Immune Microenvironment. Cell
1129 *175*, 1972–1988.e16.

1130 Ooft, S.N., Weeber, F., Dijkstra, K.K., McLean, C.M., Kaing, S., van Werkhoven, E., Schipper,
1131 L., Hoes, L., Vis, D.J., van de Haar, J., et al. (2019). Patient-derived organoids can predict
1132 response to chemotherapy in metastatic colorectal cancer patients. Sci Transl Med *11*.

1133 Preti, M.G., Bolton, T., Van De Ville, D., (2017). The dynamic functional connectome: State-
1134 of-the-art and perspectives. Neuroimage, *160*:41-54.

1135 Rigau, M., Ostrouska, S., Fulford, T.S., Johnson, D.N., Woods, K., Ruan, Z., McWilliam,
1136 H.E.G., Hudson, C., Tutuka, C., Wheatley, A.K., et al. (2020). Butyrophilin 2A1 is essential
1137 for phosphoantigen reactivity by γδ T cells. Science *367*.

1138 Rios, A.C., Clevers, H. (2018) Imaging organoids: a bright future ahead. Nat Methods *15*, 24-
1139 26

1140 Sachs, N., et al. (2018). A Living Biobank of Breast Cancer Organoids Captures Disease
1141 Heterogeneity. Cell *172*, 373-368.e10

1142 Schafer, S.T., Paquola, A.C.M., Stern, S., Gosselin, D., Ku, M., Pena, M., Kuret, T.J.M.,
1143 Liyanage, M., Mansour, A.A., Jaeger, B.N., et al. (2019). Pathological priming causes
1144 developmental gene network heterochronicity in autistic subject-derived neurons. Nat
1145 Neurosci *22*, 243–255.

1146 Scheper, W., Gründer, C., Straetemans, T., Sebestyen, Z., and Kuball, J. (2013). Hunting for
1147 clinical translation with innate-like immune cells and their receptors. Leukemia *28*, 1181–1190.

1148 Schnalzger, T.E., de Groot, M.H., Zhang, C., Mosa, M.H., Michels, B.E., Röder, J., Darvishi,
1149 T., Wels, W.S., and Farin, H.F. (2019). 3D model for CAR-mediated cytotoxicity using patient-
1150 derived colorectal cancer organoids. Embo J. *38*, e100928.

1151 Schumacher, T.N., Scheper, W., and Kvistborg, P. (2019). Cancer Neoantigens. Annu Rev
1152 Immunol *37*, 173–200.

1153 Sebestyen, Z., Prinz, I., Déchanet-Merville, J., Silva-Santos, B., and Kuball, J. (2019).
1154 Translating gammadelta (γδ) T cells and their receptors into cancer cell therapies. Nat Rev
1155 Drug Discov *32*, 1–16.

1156 Serra, D., Mayr, U., Boni, A., Lukonin, I., Rempfler, M., Challet Meylan, L., Stadler, M.B.,
1157 Strnad, P., Papasaikas, P., Vischi, D., et al. (2019). Self-organization and symmetry breaking
1158 in intestinal organoid development. Nature *569*, 66–72.

1159 Sistigu, A., Yamazaki, T., Vacchelli, E., Chaba, K., Enot, D.P., Adam, J., Vitale, I., Goubar,
1160 A., Baracco, E.E., Remédios, C., et al. (2014). Cancer cell-autonomous contribution of type I
1161 interferon signaling to the efficacy of chemotherapy. Nat. Med. *20*, 1301–1309.

1162 Straetemans, T., Gründer, C., Heijhuurs, S., Hol, S., Slaper-Cortenbach, I., Bönig, H.,
1163 Sebestyen, Z., and Kuball, J. (2015). Untouched GMP-Ready Purified Engineered Immune
1164 Cells to Treat Cancer. Clin. Cancer Res. *21*, 3957–3968.

1165 Straetemans, T., Kierkels, G.J.J., Doorn, R., Jansen, K., Heijhuurs, S., Santos, Dos, J.M., van
1166 Muyden, A.D.D., Vie, H., Clemenceau, B., Raymakers, R., et al. (2018). GMP-Grade
1167 Manufacturing of T Cells Engineered to Express a Defined γδTCR. Front. Immunol. *9*, 1062.

1168 Stuart, T., Butler, A., Hoffman, P., Hafemeister, C., Papalexi, E., Mauck, W.M., Hao, Y.,
1169 Stoeckius, M., Smibert, P., and Satija, R. (2019). Comprehensive Integration of Single-Cell
1170 Data. Cell *177*, 1888–1902.e21.

1171 Szabo, P.A., Levitin, H.M., Miron, M., Snyder, M.E., Senda, T., Yuan, J., Cheng, Y.L., Bush,
1172 E.C., Dogra, P., Thapa, P., et al. (2019). Single-cell transcriptomics of human T cells reveals
1173 tissue and activation signatures in health and disease. Nat Commun *10*, 4706–4716.

1174 Tan, T.C.J., Knight, J., Sbarrato, T., Dudek, K., Willis, A.E., and Zamoyska, R. (2017).
1175 Suboptimal T-cell receptor signaling compromises protein translation, ribosome biogenesis,
1176 and proliferation of mouse CD8 T cells. Proc. Natl. Acad. Sci. U.S.A. *114*, E6117–E6126.

1177 Terrier, B., Bièche, I., Maisonobe, T., Laurendeau, I., Rosenzwajg, M., Kahn, J.-E., Diemert,
1178 M.-C., Musset, L., Vidaud, M., Sène, D., et al. (2010). Interleukin-25: a cytokine linking
1179 eosinophils and adaptive immunity in Churg-Strauss syndrome. Blood *116*, 4523–4531.

1180 Tiriac, H., Belleau, P., Engle, D.D., Plenker, D., Deschênes, A., Somerville, T.D.D., Froeling,
1181 F.E.M., Burkhart, R.A., Denroche, R.E., Jang, G.-H., et al. (2018). Organoid Profiling
1182 Identifies Common Responders to Chemotherapy in Pancreatic Cancer. Cancer Discov *8*,
1183 1112–1129.

1184 Tuveson, D., Clevers, H. (2019) Cancer modeling meets human organoid technology. Science
1185 *364*, 952-955.

1186 Van Acker, H.H., Capsomidis, A., Smits, E.L., and Van Tendeloo, V.F. (2017). CD56 in the
1187 Immune System: More Than a Marker for Cytotoxicity? Front. Immunol. *8*, 892.

1188 Van der Leun, A.M., Thommen, D.S., and Schumacher, T.N. (2020). CD8+ T cell states in
1189 human cancer: insights from single-cell analysis. Nat. Rev. Cancer *20*, 218–232.

1190 Van Ineveld et al. mLSR-3D and STAPL-3D reveals the spatio-phenotypic patterning of cells
1191 in healthy and tumor tissues. Nat. Biotechnol, *in press*.

1192 Vlachogiannis, G., Hedayat, S., Vatsiou, A., Jamin, Y., Fernández-Mateos, J., Khan, K.,
1193 Lampis, A., Eason, K., Huntingford, I., Burke, R., et al. (2018). Patient-derived organoids
1194 model treatment response of metastatic gastrointestinal cancers. Science *359*, 920–926.

1195 Vyborova, A., et al. (2020). γ9δ2T cell diversity and the receptor interface with tumor cells. J.
1196 Clin. Invest. *130*, 4637-4651

1197 Weigelin, B., et al. (2020) Cancer cell elimination by cytotoxic T cell cooperation and additive
1198 damage. BioRxiv 2020.04.22.054718

1199 Wilkinson, L. (2011). ggplot2: elegant graphics for data analysis by WICKHAM, H.
1200 doi:10.1111/j.1541-0420.2011.01616.x

1201 Yamamoto, T.N., Kishton, R.J., and Restifo, N.P. (2019). Developing neoantigen-targeted T
1202 cell-based treatments for solid tumors. Nat. Med. *25*, 1488–1499.

1203 Yao, Y., Xu, X., Yang, L., Zhu, J., Wan, J., Shen, L., Xia, F., Fu, G., Deng, Y., Pan, M., et al.
1204 (2020). Patient-Derived Organoids Predict Chemoradiation Responses of Locally Advanced
1205 Rectal Cancer. Cell Stem Cell *26*, 17–26.e6.

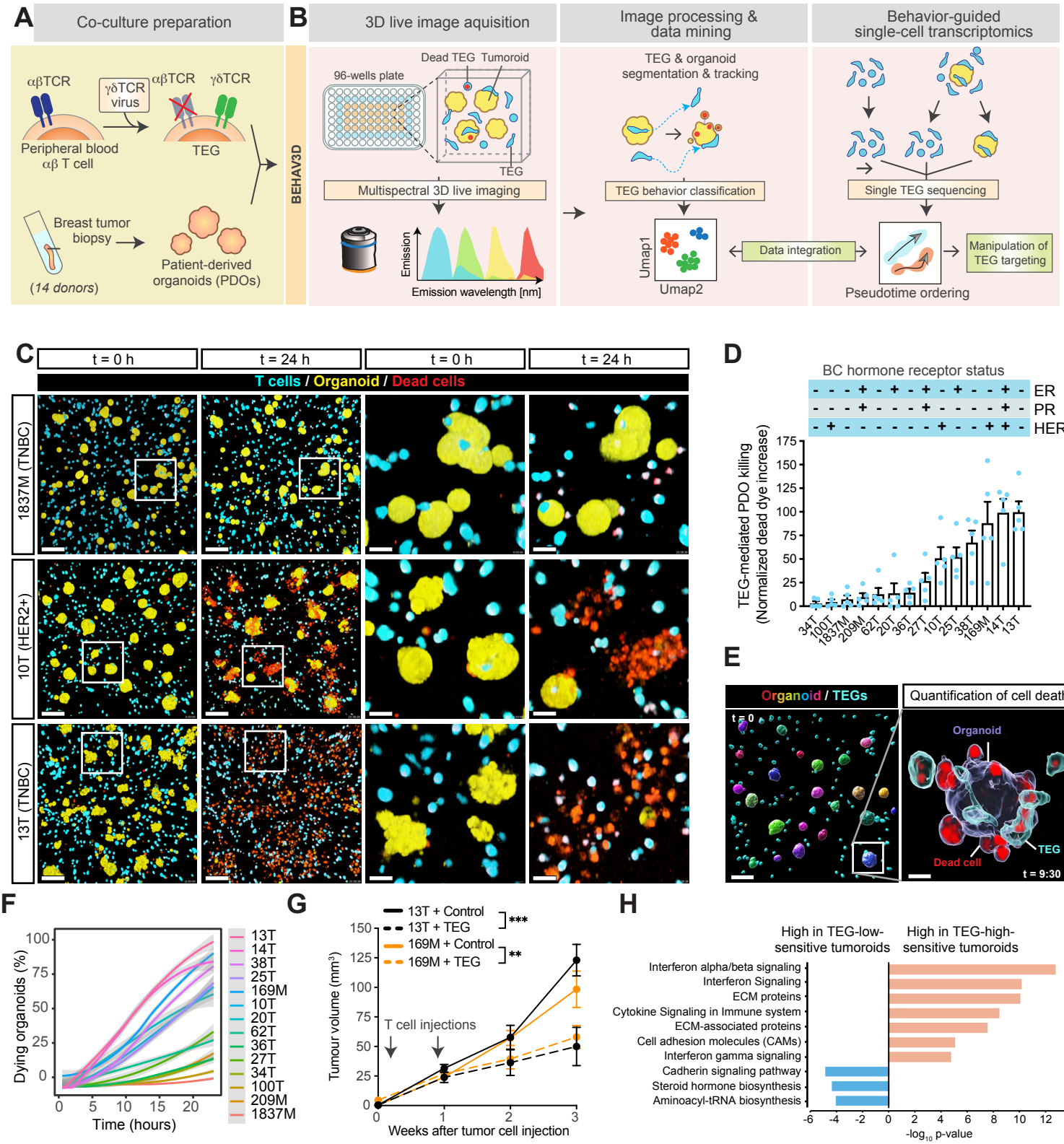
A
Co-culture preparation
αβTCR
γδTCR virus
αβTCR
γδTCR
Peripheral blood αβ T cell
TEG
Breast tumor biopsy
Patient-derived organoids (PDOs)
(14 donors)
B
3D live image aquisition
Image processing & data mining
Behavior-guided single-cell transcriptomics
BEHAV3D
96-wells plate
Dead TEG
Tumoroid
TEG
Multispectral 3D live imaging
Emission
Emission wavelength [nm]
TEG & organoid segmentation & tracking
TEG behavior classification
Umap1
Umap2
Data integration
Single TEG sequencing
Pseudotime ordering
Manipulation of TEG targeting
C
t = 0 h
t = 24 h
t = 0 h
t = 24 h
T cells / Organoid / Dead cells
1837M (TNBC)
10T (HER2+)
13T (TNBC)
D
BC hormone receptor status
ER
PR
HER2
TEG-mediated PDO killing (Normalized dead dye increase)
34T
100T
1837M
209M
62T
20T
36T
27T
10T
25T
38T
169M
14T
13T
E
Organoid / TEGs
Quantification of cell death
t = 0
Organoid
TEG
Dead cell
t = 9:30 h
F
Dying organoids (%)
Time (hours)
13T
14T
38T
25T
169M
10T
20T
62T
36T
27T
34T
100T
209M
1837M
G
13T + Control
13T + TEG
169M + Control
169M + TEG
***
**
T cell injections
Tumour volume (mm³)
Weeks after tumor cell injection
H
High in TEG-low-sensitive tumoroids
High in TEG-high-sensitive tumoroids
Interferon alpha/beta signaling
Interferon Signaling
ECM proteins
Cytokine Signaling in Immune system
ECM-associated proteins
Cell adhesion molecules (CAMs)
Interferon gamma signaling
Cadherin signaling pathway
Steroid hormone biosynthesis
Aminoacyl-tRNA biosynthesis
-log10 p-value

Figure 1

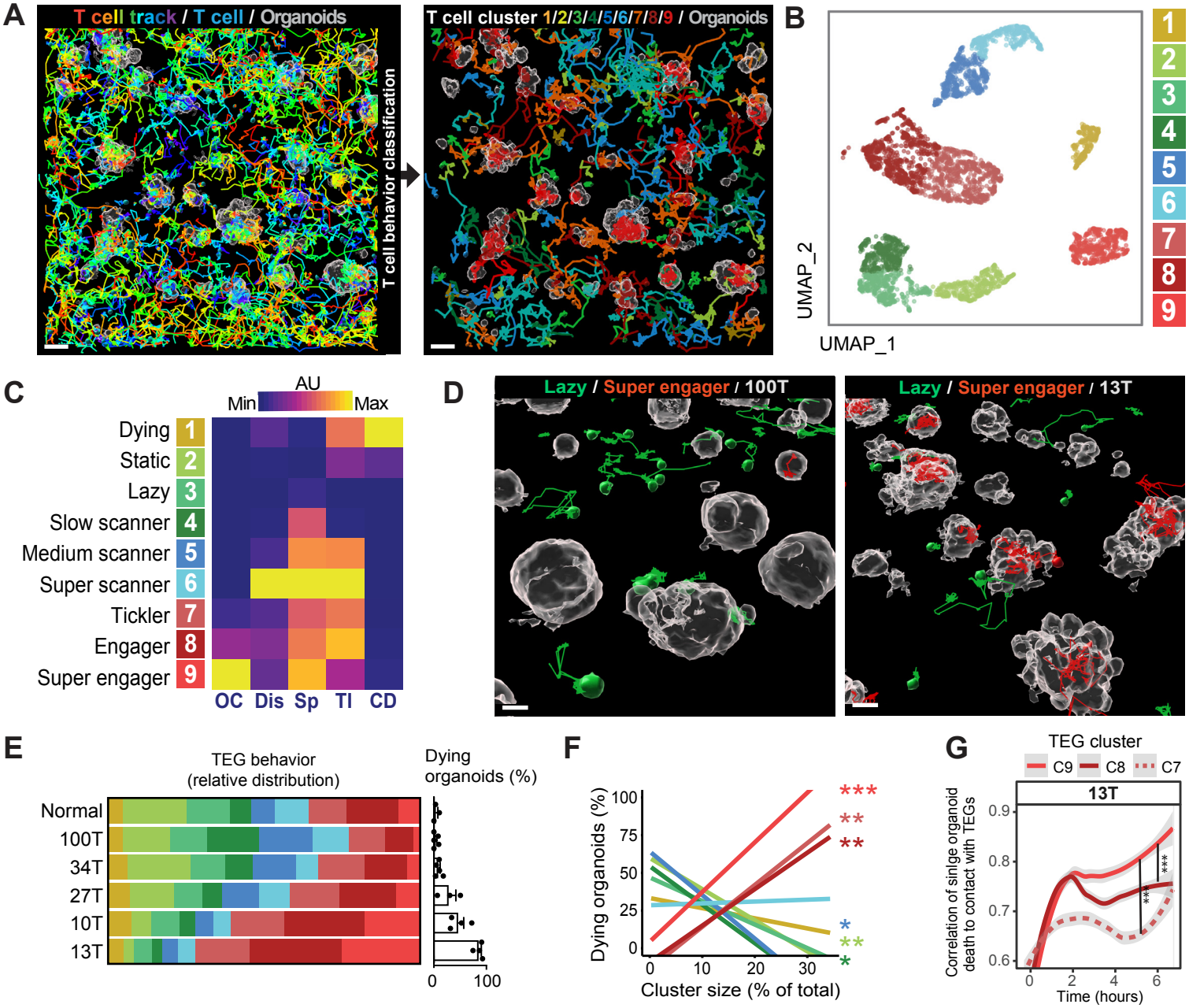
A
T cell track / T cell / Organoids
T cell behavior classification
T cell cluster 1/2/3/4/5/6/7/8/9 / Organoids
B
UMAP_2
UMAP_1
1
2
3
4
5
6
7
8
9
C
AU
Min
Max
Dying 1
Static 2
Lazy 3
Slow scanner 4
Medium scanner 5
Super scanner 6
Tickler 7
Engager 8
Super engager 9
OC Dis Sp Tl CD
D
Lazy / Super engager / 100T
Lazy / Super engager / 13T
E
TEG behavior
(relative distribution)
Dying
organoids (%)
Normal
100T
34T
27T
10T
13T
0
100
F
Dying organoids (%)
100
75
50
25
0
0 10 20 30
Cluster size (% of total)
***
**
**
*
**
*
G
TEG cluster
C9 C8 C7
13T
Correlation of sinlge organoid death to contact with TEGs
0.9
0.8
0.7
0.6
0 2 4 6
Time (hours)
***
***

Figure 2

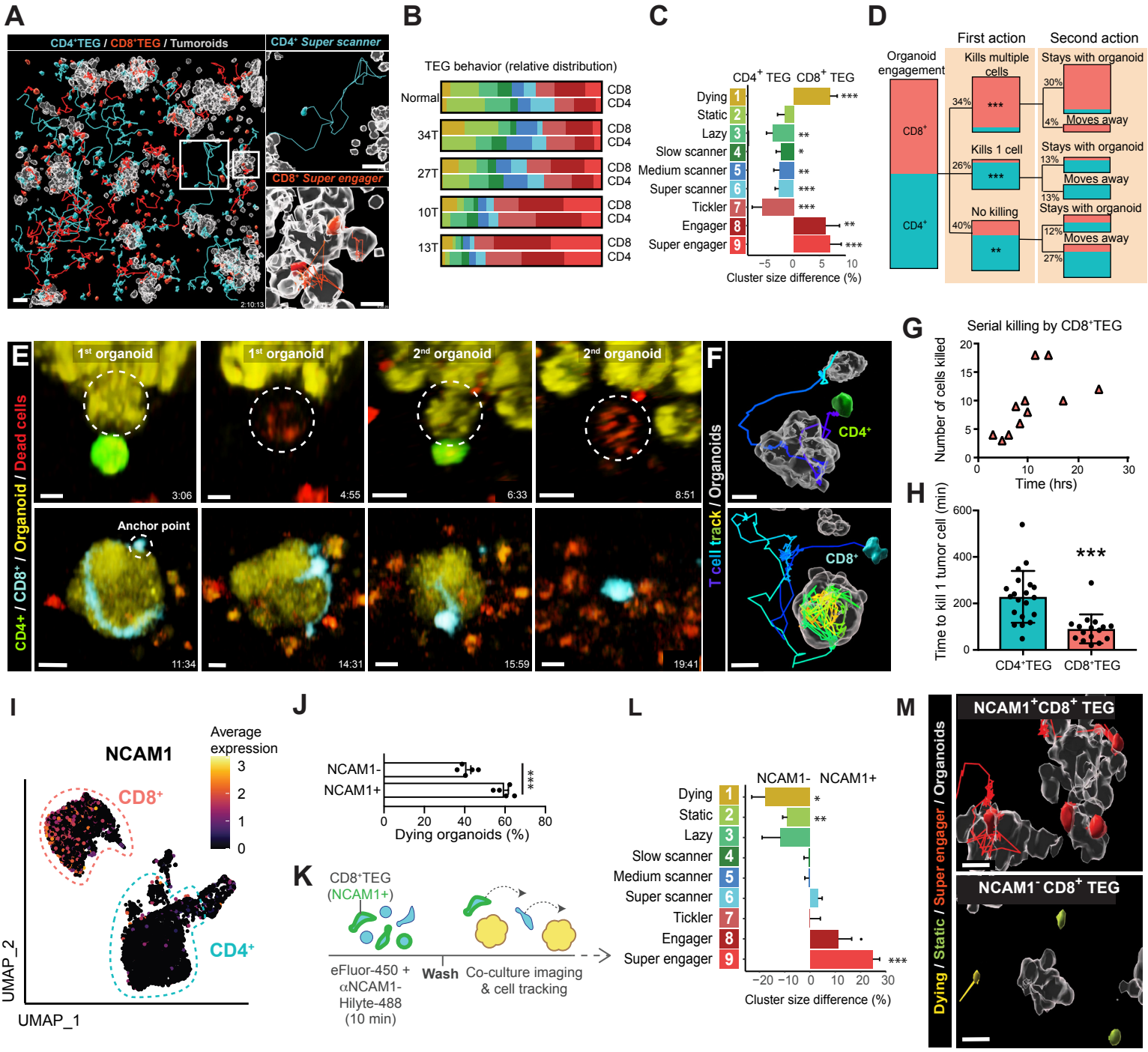
A
CD4+TEG / CD8+TEG / Tumoroids
CD4+ Super scanner
CD8+ Super engager
B
TEG behavior (relative distribution)
Normal
34T
27T
10T
13T
CD8
CD4
C
CD4+ TEG CD8+ TEG
Dying
Static
Lazy
Slow scanner
Medium scanner
Super scanner
Tickler
Engager
Super engager
Cluster size difference (%)
D
First action
Second action
Organoid engagement
CD8+
CD4+
Kills multiple cells
Kills 1 cell
No killing
Stays with organoid
Moves away
E
1st organoid
2nd organoid
Anchor point
CD4+ / CD8+ / Organoid / Dead cells
F
T cell track / Organoids
CD4+
CD8+
G
Serial killing by CD8+TEG
Number of cells killed
Time (hrs)
H
Time to kill 1 tumor cell (min)
CD4+TEG
CD8+TEG
I
NCAM1
Average expression
CD8+
CD4+
UMAP_2
UMAP_1
J
NCAM1-
NCAM1+
Dying organoids (%)
K
CD8+TEG (NCAM1+)
eFluor-450 + αNCAM1-Hilyte-488 (10 min)
Wash
Co-culture imaging & cell tracking
L
NCAM1-
NCAM1+
Cluster size difference (%)
M
NCAM1+CD8+ TEG
NCAM1-CD8+ TEG
Dying / Static / Super engager / Organoids

Figure 3

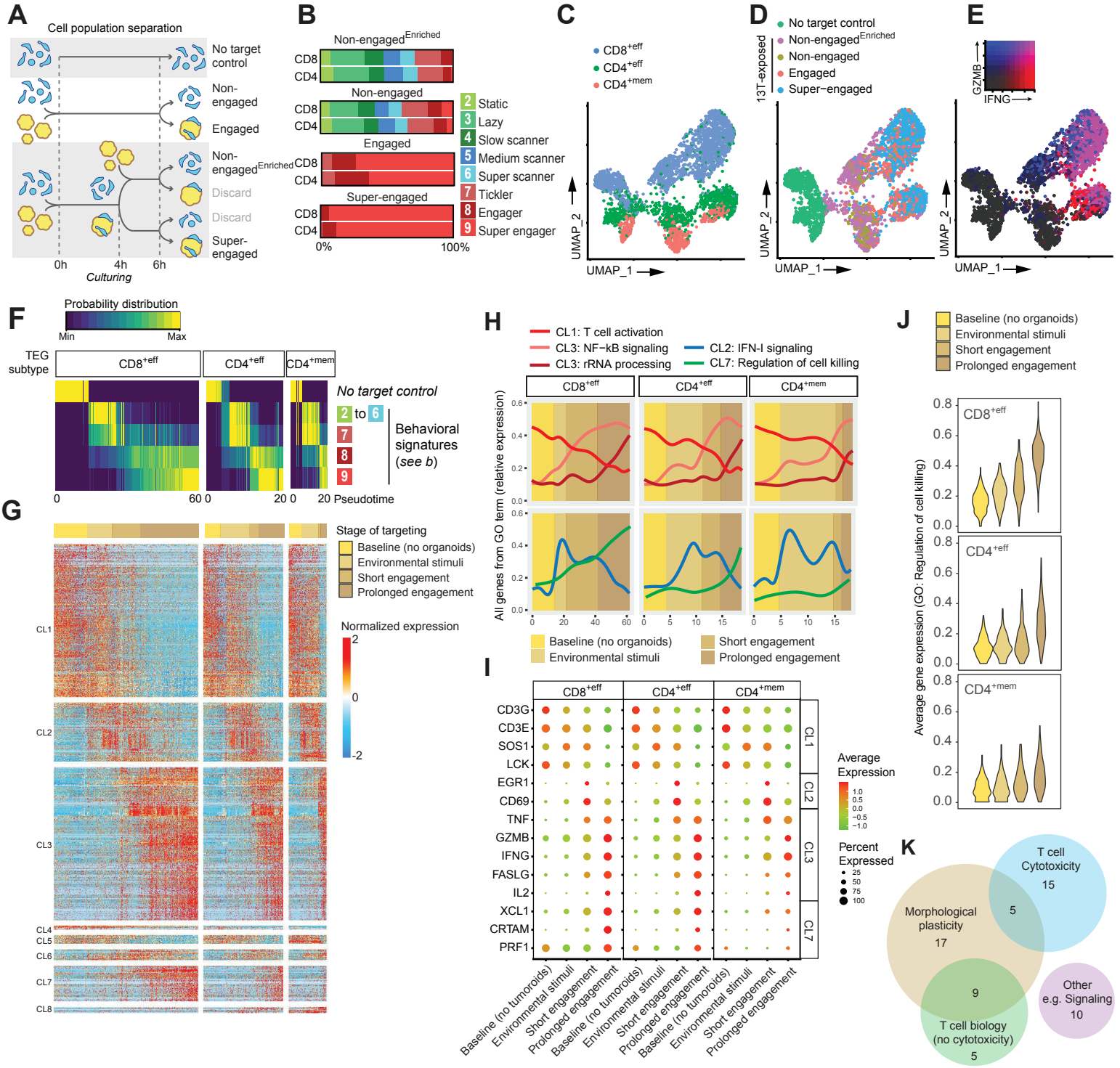
A
Cell population separation
No target control
Non-engaged
Engaged
Non-engaged Enriched
Discard
Discard
Super-engaged
0h
4h
6h
Culturing
B
Non-engaged Enriched
Non-engaged
Engaged
Super-engaged
CD8
CD4
0%
100%
2 Static
3 Lazy
4 Slow scanner
5 Medium scanner
6 Super scanner
7 Tickler
8 Engager
9 Super engager
C
CD8+eff
CD4+eff
CD4+mem
UMAP_1
UMAP_2
D
No target control
Non-engaged Enriched
Non-engaged
Engaged
Super-engaged
13T-exposed
E
GZMB
IFNG
F
Probability distribution
Min
Max
TEG subtype
CD8+eff
CD4+eff
CD4+mem
No target control
2 to 6
7
8
9
Behavioral signatures (see b)
Pseudotime
G
Stage of targeting
Baseline (no organoids)
Environmental stimuli
Short engagement
Prolonged engagement
Normalized expression
CL1
CL2
CL3
CL4
CL5
CL6
CL7
CL8
H
CL1: T cell activation
CL3: NF−kB signaling
CL3: rRNA processing
CL2: IFN-I signaling
CL7: Regulation of cell killing
All genes from GO term (relative expression)
Baseline (no organoids)
Environmental stimuli
Short engagement
Prolonged engagement
I
CD3G
CD3E
SOS1
LCK
EGR1
CD69
TNF
GZMB
IFNG
FASLG
IL2
XCL1
CRTAM
PRF1
Average Expression
Percent Expressed
J
Baseline (no organoids)
Environmental stimuli
Short engagement
Prolonged engagement
Average gene expression (GO: Regulation of cell killing)
K
T cell Cytotoxicity
15
Morphological plasticity
17
5
9
Other e.g. Signaling
10
T cell biology (no cytotoxicity)
5

Figure 4

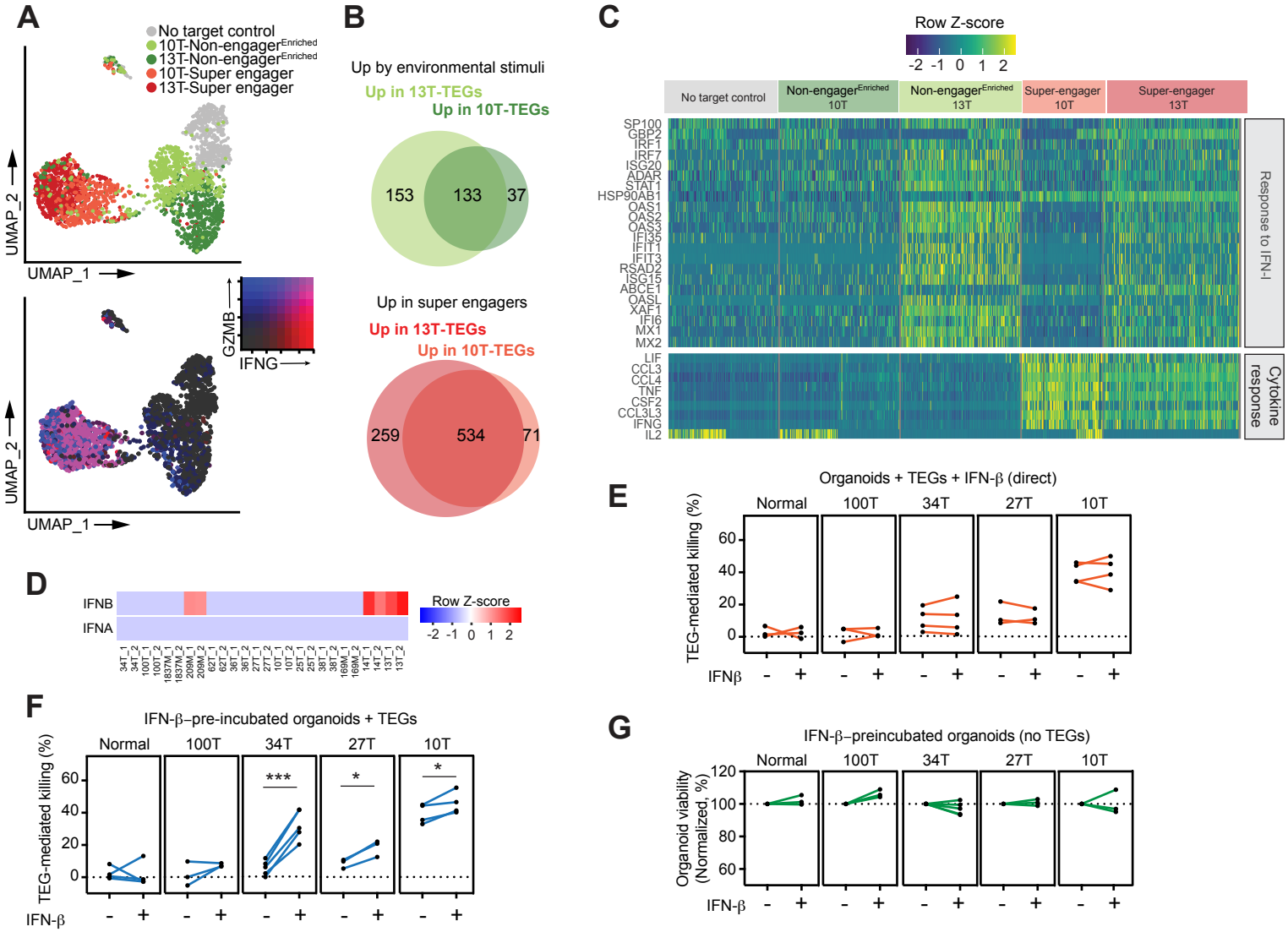
A
No target control
10T-Non-engager Enriched
13T-Non-engager Enriched
10T-Super engager
13T-Super engager
UMAP_2
UMAP_1
GZMB
IFNG
B
Up by environmental stimuli
Up in 13T-TEGs
Up in 10T-TEGs
153
133
37
Up in super engagers
Up in 13T-TEGs
Up in 10T-TEGs
259
534
71
C
Row Z-score
-2 -1 0 1 2
No target control
Non-engager Enriched 10T
Non-engager Enriched 13T
Super-engager 10T
Super-engager 13T
SP100
GBP2
IRF1
IRF7
ISG20
ADAR
STAT1
HSP90AB1
OAS1
OAS2
OAS3
IFI35
IFIT1
IFIT3
RSAD2
ISG15
ABCE1
OASL
XAF1
IFI6
MX1
MX2
LIF
CCL3
CCL4
TNF
CSF2
CCL3L3
IFNG
IL2
Response to IFN-I
Cytokine response
D
IFNB
IFNA
Row Z-score
-2 -1 0 1 2
E
Organoids + TEGs + IFN-β (direct)
Normal
100T
34T
27T
10T
TEG-mediated killing (%)
IFNβ
F
IFN-β–pre-incubated organoids + TEGs
Normal
100T
34T
27T
10T
TEG-mediated killing (%)
***
*
*
IFN-β
G
IFN-β–preincubated organoids (no TEGs)
Normal
100T
34T
27T
10T
Organoid viability (Normalized, %)
IFN-β

Figure 5